This is a preprint, the final version is subject to change, of the American Mineralogist (MSA)
Cite as Authors (Year) Title. American Mineralogist, in press.
(DOI will not work until issue is live.) DOI: http://dx.doi.org/10.2138/am-2017-5885

Revision1

Cu and Fe diffusion in rhyolitic melts during chalcocite "dissolution": Implications for porphyry ore deposits and tektites

Peng Ni[1*], Youxue Zhang[1], Adam Simon[1], Joel Gagnon[2]

[1]Department of Earth and Environmental Sciences, University of Michigan, Ann Arbor, MI 48109-1005, USA

[2]Department of Earth and Environmental Sciences, University of Windsor, Windsor, ON, N9B 3P4, Canada

ABSTRACT

Copper diffusion plays an important role in natural processes, such as metal transport during the formation of magmatic-hydrothermal porphyry-type ore deposit and Cu isotope fractionation during tektite formation. Copper diffusion data in natural silicate melts, however, are limited. In this study, chalcocite (Cu_2S) "dissolution" experiments were carried out by using chalcocite-rhyolite diffusion "couples" to study Cu (and S) diffusion in rhyolitic melts. Instead of chalcocite dissolution as initially expected, our experiments show that Cu is transferred from the chalcocite crystal to the rhyolitic melt, and Fe is transferred from the rhyolitic melt to chalcocite, whereas the S concentration profile in the rhyolitic melt is essentially flat. From the Cu and Fe exchange profiles in the rhyolitic melts, Cu diffusivities and Fe diffusivities are obtained and reported.

Copper diffusivity in rhyolitic melts containing 0.10 to 5.95 wt% H_2O at temperatures of 750 to 1391ºC and pressures of 0.5 to 1.0 GPa can be described as:

$$D_{Cu}^{Rhy} = \exp\left[-(14.75\pm0.35)-(0.23\pm0.10)w-\frac{(11647\pm491)-(698\pm117)w}{T}\right],$$

*Corresponding author. *E-mail address*: pengni@umich.edu

which allows the estimation of an activation energy for diffusion in dry rhyolitic melts to be 96.8±4.1 kJ/mol. In the above equation, diffusivity (D) is in m^2/s, T is the temperature in K, w is the H_2O concentration in the rhyolitic melts in wt% and all errors reported are at 1σ level. Combining Cu diffusion data from this study and previous data in basaltic melt gives a general equation for Cu diffusivity in natural silicate melts:

$$D_{\mathrm{Cu}} = \exp\left[-(17.3\pm0.9)+(3.8\pm1.5)(\mathrm{Si+Al-H})-\frac{(4403\pm1094)+(9700\pm1921)(\mathrm{Si+Al-H})}{T}\right],$$

where Si+Al-H is the cation mole fraction of Si plus Al minus H in the silicate melt on a wet basis.

Iron diffusivities obtained in this study in anhydrous to 6 wt% H_2O rhyolite are combined with previous data to get a general equation for Fe diffusion in rhyolitic melts:

$$D_{\mathrm{Fe}}^{\mathrm{Rhy}} = \exp\left[-(16.1\pm1.7)-\frac{(19859\pm2541)-(1218\pm135)w}{T}\right].$$

Our data demonstrate that Cu diffusion is faster than H_2O or Cl in rhyolitic melts containing 6 wt% water, which indicates that the scavenging and transport of Cu by a magmatic volatile phase during formation of porphyry-type ore deposits is not limited by diffusion of Cu. Based on our experimental data, Cu diffusivity is almost 4 orders of magnitude higher than Zn in anhydrous rhyolitic melts, which supports the explanation of more diffusive loss of Cu leading to more fractionated Cu isotopes than Zn isotopes in tektites.

Key words: copper diffusion, iron diffusion, porphyry-type deposits, kinetic fractionation

This is a preprint, the final version is subject to change, of the American Mineralogist (MSA)
Cite as Authors (Year) Title. American Mineralogist, in press.
(DOI will not work until issue is live.) DOI: http://dx.doi.org/10.2138/am-2017-5885

INTRODUCTION

Porphyry-type ore deposits are important sources for metals, such as Cu, Au, Mo and Ag, comprising~57%, 10%, 99% and 13%, respectively, of the world's total discovered quantities of these metals (Singer 1995). In order to form a porphyry-Cu deposit, the Cu concentration must be enriched from a crustal average concentration of ~30 ppm (Rudnick and Gao 2014) to a typical mineable grade of ~0.2 to 2 wt% in the porphyry environment (Simon and Ripley 2011). This 2 to 3 orders of magnitude enrichment is accomplished by, among other things, the efficient scavenging of Cu by a magmatic volatile phase (MVP) exsolved from silicate melts in Earth's upper continental crust (e.g. Candela 1997; Wilkinson 2013). The exsolution of an MVP from silicate melts can occur by decompression, which reduces the solubility of volatiles in the melt (i.e., first boiling; Audetat and Simon 2012), or crystal fractionation that occurs during cooling of magma in shallow level magma chambers (i.e., second boiling, Candela 1997; Audetat and Simon 2012). Since the exsolved MVP bubbles are less dense than the surrounding silicate magma, at a volume fraction >10% the bubbles can form an interconnected network and rise through the magma chamber (Candela 1991; Parmigiani et al. 2016), simultaneously scavenging ore metals, such as Cu, Au, Mo and Ag from the surrounding melt, and possibly also via resorption of metal sulfides (Audetat and Simon 2012). Huber et al. (2012) quantitatively modeled the partitioning and transport of metals by an MVP that ascends through a magma chamber, and determined that the efficiency of metal extraction (i.e., the total quantity of a metal removed from the magma chamber and transported into the overlying porphyry environment) is dependent on a balance between diffusion of the metal in the silicate melt, and the advection of the MVP through the magma chamber. They showed that elements with high diffusivities will more likely reach equilibrium with the MVP and be efficiently transported, whereas elements

with low diffusivities might not equilibrate with a rapidly ascending MVP and, therefore, become less efficiently scavenged and transported. Such an effect can lead to diffusive fractionation of metals, and hence variability of metal ratios in magmatic-hydrothermal ore deposits.

Moynier et al. (2009, 2010) studied Cu and Zn isotope systematics in tektites, and found that Cu isotopes are more fractionated than Zn isotopes in the same batch of tektites. The fractionation of Cu and Zn isotopes in tektites can be explained by the evaporative loss of Cu and Zn from the tektites during their formation, when a short period of high temperature was experienced (as high as >2800 ºC, Walter 1967). However, if condensation temperature alone controlled isotope fractionation, the greater degree of fractionation of Cu isotopes relative to Zn isotopes is inconsistent with the lower half condensation temperature of Zn ($T_{1/2}$ ~ 726 K, Lodders 2003) than Cu ($T_{1/2}$ ~ 1037 K, Lodders 2003). The authors invoked a "diffusion-limited" mechanism, and suggested that the more fractionated Cu isotope signature is due to the higher diffusivity of Cu^{+} than Zn^{2+} in silicate melt. The higher diffusivity of Cu would lead to more rapid loss of Cu from the tektite during heating, and would result in more fractionated Cu isotopes than Zn isotopes in tektites.

Despite the potential role of Cu diffusion in magmatic-hydrothermal porphyry-type ore formation and tektite and other isotope fractionation processes, Cu diffusion data are limited. To our knowledge, only two experimental studies on Cu diffusion have been conducted. Von der Gonna and Russel (2000) studied Cu diffusion in a $Na_2O{\cdot}2SiO_2$ melt using a voltammetry method. Ni and Zhang (2016) investigated Cu diffusion in anhydrous basaltic melt by the diffusion couple method. Because porphyry-type deposits typically originate from water-saturated intermediate to felsic magmas (Simon and Ripley 2011), and tektites are often

87 "rhyolitic" in terms of their silica content (e.g., Cassidy et al. 1969), Cu diffusion data from these
88 two studies cannot be directly applied to elucidate the evolution of porphyry-type ore deposits or
89 isotope fractionation in tektites. In this study, we report Cu diffusion data in rhyolitic melts
90 containing 0.1 to 5.9 wt% H_2O from chalcocite "dissolution" experiments, and discuss the
91 implications of the data in the context of natural processes of porphyry-type Cu deposit
92 formation and Cu isotope fractionation in tektites.

93

94 ## EXPERIMENTAL AND ANALYTICAL METHODS

95 ### Starting materials

96 In this study, chalcocite "dissolution" experiments were carried out to determine Cu
97 diffusivities over the temperature range of 750 ºC to 1391 ºC in silicate melts with rhyolitic
98 compositions and with H_2O concentrations ranging from "anhydrous" (0.10 ~ 0.24 wt%) to 5.9
99 wt%. "Dissolution" is referred to in quotation marks because, even though the experiments were
100 initially designed as chalcocite dissolution to study the diffusion of both Cu and S, the actual
101 chemical reaction observed in our experiments is close to "metal exchange" as discussed below.

102 A cluster of chalcocite (Cu_2S) crystals purchased from a gem dealer was used as the
103 starting material. As examined using scanning electron microscope (SEM) and election
104 microprobe (EMP), the chalcocite crystals are mostly pure Cu_2S (20.36 wt% S, 81.10 wt% Cu
105 and 0.00 wt% Fe), but occasionally have inclusions of bornite (Cu_5FeS_4) and Cu metal
106 (compositions plotted in Fig. 1). When preparing samples for the experiments, care was taken to
107 avoid any impurities in the chalcocite crystal. Six rhyolitic glasses with H_2O concentrations from
108 0.1 wt% to 5.9 wt% were used for this series of experiments. The major element compositions

and H_2O concentrations of the starting glasses are summarized in Table 1. Among these rhyolitic glasses, NCO is a natural glass from the Newberry Crater, Oregon; bb7b-25 is a natural obsidian glass from the Mono Crater, California; CIT is a natural obsidian glass from Coso Range, California, which was previously used for infrared (IR) spectral calibration by Newman et al. (1986); and GMR+2, GMR+4 and GMR+6 are glasses synthesized by hydration of obsidians from Glass Mountain, California, which were previously used in studies for viscosity and water speciation of rhyolites (Hui and Zhang 2007; Hui et al. 2008). The SiO_2 concentration in the rhyolites, on a dry weight basis, ranges from 73.4 to 76.7 wt% (the concentrations reported in Table 1 include H_2O). Glass cylinders rather than powders were used for the experiments. These starting glass cylinders already contain dissolved H_2O, and no liquid H_2O was added into the capsule during the experiment.

Piston cylinder experiments

In preparation for piston cylinder experiments, a chalcocite crystal and rhyolitic glass were first cut and prepared into long cylinders with a diameter of ~2 mm. A wafer was then cut from each of the cylinders, with a thickness of ~1 mm for the chalcocite wafer and 1 to 2 mm for the rhyolitic glass wafer depending on the estimated profile length for each experiment. The wafers were doubly polished with progressively finer sandpapers, finishing with 0.3-μm alumina powders. After examination under optical microscope, chalcocite and rhyolitic glass wafers with the least amount of impurities were chosen for experiments. After cleaning and drying, the wafers were placed into a graphite capsule, with the rhyolite glass on top and the denser chalcocite at the bottom. The graphite capsule was fit tightly into a drilled hole of an MgO rod, then into a graphite furnace, and finally into a barium carbonate pressure medium. Effort was

made to place the interface right at the center of the graphite furnace to minimize temperature gradients across the sample.

All piston cylinder experiments were carried out at the University of Michigan. The pressure was measured by a Heise digital pressure gauge. A 5% correction is applied to the nominal pressure based on the calibration by Ni and Zhang (2008) on the same piston cylinder apparatus. The experimental charge was pressurized to 15% above the target pressure, and then allowed to relax overnight at 200 ºC to close gaps inside the assembly. After relaxation, the sample was heated up to the target temperature in ~50 s using a programed temperature controller. Pressure was maintained manually using an Enerpac electric pump. The pressure fluctuation was within 1% during the experiment, ~10% during heating up and ~20% during quench. Temperature was measured by a Type-S thermocouple (Pt90Rh10-Pt) and controlled by a Eurotherm controller. Temperature correction based on the distance from the thermocouple tip to the interface was applied using the calibration of Hui et al. (2008). The thermocouple tip is typically 2 to 2.5 mm away from the interface. The temperature variation across the sample is usually ≤13 ºC. No temperature overshoot was observed during the experiment, and the temperature fluctuation recorded by the temperature controller was ±1 ºC during the experiment. After a designated duration, the assembly was quenched to room temperature at a rate of ~100 ºC/s by turning off the power. The whole sample assembly was recovered from the piston cylinder apparatus and preserved in epoxy. Because of the strong secondary fluorescence effect for Cu analysis by EMP as realized in the preliminary analyses (see analytical methods), the chalcocite crystal was removed from the sample charge before probe analysis. Removal of the chalcocite crystal was done by first doubly polishing the sample to a thin wafer (<1 mm thick), and then cutting through the graphite capsule and physically pushing the chalcocite out of the

sample disc with tweezers. The hole in the sample disc after chalcocite removal was filled with epoxy to better preserve the sample glass. The rhyolitic melt does not wet the chalcocite crystal, and there is typically a gap between chalcocite and glass produced by expansion of the assembly during depressurization during and after quench, thus reducing the difficulty in the removal process. The chalcocite crystal is usually a whole undamaged piece after removal, which is then preserved in a separate epoxy disc.

Analytical methods

EMP analyses of major elements. Major element compositions and Cu concentrations were analyzed in separate sessions using the CAMECA SX-100 electron microprobe at the University of Michigan. Major oxides were analyzed using a 5 nA focused beam with an accelerating voltage of 15 kV. Standards used for the analyses are: albite (ALBA) for Na, natural rhyolitic glass (VGRH) for Si, potassium feldspar (GKFS) for K, wollastonite (WOLL) for Ca, synthetic ferrosilite (FESI) for Fe, synthetic geikielite (GEIK) for Ti, forsterite (FOBO) for Mg and sillimanite (SILL) for Al. Counting time for each element was 20 to 40 seconds on the peak, and 10 to 20 seconds on each side of the background. A special routine was employed for counting Na (extrapolating to photon counts at zero time) to correct for Na loss during analysis.

Secondary fluorescence effect in EMP analysis for Cu. Although the strong secondary fluorescence effect on Cu analysis using EMP was avoided by removing chalcocite crystal from the capsule after experiment, a brief description of the effect is included below as a reference for future studies. Our test analyses before we decided to remove chalcocite from the experimental charge show that secondary fluorescence effect is a significant concern in EMP analysis for trace

178 amount of Cu (i.e. hundreds of ppm) when a Cu-rich phase is within hundreds of micrometers of
179 the analytical spot. In our test analyses, a chalcocite wafer and a rhyolitic glass wafer (CIT) were
180 polished and placed into a graphite capsule, then preserved in epoxy and polished to the center
181 section for EMP analysis. Traverses were measured in the glass perpendicular to the contact
182 between the chalcocite crystal and the glass, and the results are plotted in Fig. 2a (Line 1 through
183 Line 3). The results show that the secondary fluorescence effect for Cu is especially large in
184 EMP analysis compared to other elements such as Zr (Harrison and Watson 1983; Zhang and Xu
185 2016), Cr (Zhao et al. 2015), and Sn (Yang et al. 2016), for example. Copper concentration in
186 this natural glass is low and roughly uniform (2.7±1.1 ppm, based on analyses of Chal-Rhy-4-2).
187 The secondary fluorescence profile, however, yields over 6000 ppm Cu near the contact with the
188 chalcocite, 1000 ppm Cu at 100-μm distance away from the chalcocite, and extends more than
189 200 μm into the glass (Fig. 2a).

190 Secondary fluorescence effect for Cu analysis was also estimated by Monte Carlo
191 simulations using the software package PENEPMA (Llovet and Salvat 2008). The geometry
192 used in the simulation was set up following the sample orientation, where a chalcocite crystal
193 (Cu_2S) and a rhyolitic glass (CIT) were placed on a plane right next to each other. The electron
194 beam was applied perpendicular to the glass surface with an initial energy of 15 keV. Movement
195 of the electrons and all secondary particles and X-rays was tracked until their energies were
196 below 7 keV. A pseudo-spectrometer covering the entire sample surface was used to record X-
197 ray spectra from 7 kV to 15 kV. About 5 million electrons were simulated at each spot to achieve
198 a statistical precision of ~1% on the Cu Kα peaks. Then the X-ray spectra obtained from Monte
199 Carlo simulations were convolved assuming a spectral resolution of 40 eV, after which the peak
200 heights of Cu Kα were measured. The same simulation was run on a target of Cu metal as the

standard, and peak count ratios on sample over standard are plotted in Fig. 2b, and compared to EMP measurements by three wavelength-dispersive X-ray spectrometers. Two key conclusions can be drawn from the comparison. Firstly, the Monte Carlo simulation matches the measurements well. Secondly, the secondary fluorescence effect on each WDS detector is different based on its relative orientation to the sample (Fig. 2b). According to the measurements, the WDS detector records higher counts of secondary fluorescence signal of Cu Kα if the chalcocite side of the couple is facing the detector (Spectrometer 4). This phenomenon is similar to the findings of a previous study on secondary fluorescence effect of Nb Kα in an Nb-Pd_2HfAl couple (Fournelle et al. 2005). One possible explanation is that chalcocite has a smaller mass attenuation coefficient for Cu Kα than rhyolitic glass, so that more Cu Kα X-rays survived the pathway through the chalcocite crystal and reached the detector.

The Cu diffusion profiles in our samples are typically hundreds of micrometers long, with an interface concentration of less than 1000 ppm. The strong secondary fluorescence effect completely overwhelms the actual Cu diffusion profile (Fig. 2a, Line 4). Hence, we decided to remove chalcocite from our sample charge after experiment for precise EMP analysis of Cu.

EMP analyses of Cu. With chalcocite removed, Cu concentrations were measured on glass in dedicated EMP sessions for Cu alone with three spectrometers counting Cu Kα peak for 240 s at the same time, and then 120 s counting on background on each side of the peak. A focused beam was used for the anhydrous rhyolite glasses (NCO and CIT), while a 10 μm scanning beam was used for the hydrous glasses (bb7b-25, GMR+2, GMR+4 and GMR+6) to minimize the beam damage during the analysis. The beam current was 40 nA when the interface Cu concentrations were high (e.g. higher than 500 ppm), achieving a detection limit of ~80 ppm. Otherwise a beam

current of 100 nA was used to achieve a detection limit of ~50 ppm for Cu. Previously analyzed major element compositions of the glasses (Table 1) were input into the software for ZAF correction. NIST SRM 610 was used as a secondary standard to verify the EMP analysis of Cu. The reported Cu concentration in NIST 610 is 421.7 ppm (Pearce et al. 1997), and our analyses yielded 420 to 540 ppm Cu during different sessions for this standard, indicating that EMP analyses of Cu may have systematic errors up to 120 ppm. EMP data of Cu concentrations are relatively low in precision compared to Laser-ablation ICP-MS (see below), but have higher spatial resolution (<10μm), which helps to capture the short quench profile near the interface. In addition, the multiple electron microprobe traverses verifies the horizontal homogeneity and help to rule out the concern of convection in our experiments.

Laser-ablation ICP-MS analyses of Cu. Copper concentration profiles were also analyzed using laser ablation inductively coupled plasma mass spectrometry (LA-ICP-MS) at the University of Windsor. All LA-ICP-MS data reported in this study were analyzed by using a PhotonMachines Analyte Exicite 193 nm, short-pulse-width (sub 4 ns), Ar-F excimer laser ablation system coupled with an Agilent 7900, fast-scanning quadrupole ICP-MS. The operating conditions are summarized in Table 2.

Copper concentration profiles were obtained by analyzing multiple spots along a traverse perpendicular to the interface. For each spot analysis, a 25-μm-diameter laser beam was used to ablate the sample surface at a frequency of 25 Hz for a duration of 30 s. The first few seconds of each transient laser signal were excluded during data processing to eliminate possible signal contribution from surface contamination (Pettke et al. 2012). NIST 610 synthetic glass standard was analyzed at least every hour for use as an external calibration standard and to assess

247 instrumental drift. The isotope ^{44}Ca was used as the internal calibration standard to compensate
248 for differences in ablation behavior between calibration standards and unknowns, and to obtain
249 Cu concentrations. A detection limit of ~ 0.04 ppm for Cu was achieved for our analysis using
250 the operating conditions presented in Table 2.
251
252 **FTIR analyses.** Concentrations of H_2O in the starting glasses and in glasses after diffusion
253 experiments were measured using a Perkin-Elmer GX Fourier Transform Infrared
254 Spectrometer (FTIR) at the University of Michigan. Sample glasses were typically doubly
255 polished to ~500 μm thickness for analysis. An NIR source and a CaF_2 beamsplitter were
256 used. Molecular water and OH concentrations were determined by measuring the absorption
257 peaks at 5230 and 4515 cm^{-1} respectively. The baselines were fit with a flexi curve as shown
258 in Zhang et al. (1997). Total H_2O concentrations were obtained by summing the
259 concentrations of both species calculated by using calibrated molar absorptivities from
260 Newman et al. (1986).
261 To assess possible H_2O loss during the experiments, the H_2O concentration was
262 measured in hydrous glass after the highest-temperature experiments at each H_2O
263 concentration (Chal-Rhy-1-2, Chal-Rhy-3-1, Chal-Rhy-7-1 and Chal-Rhy-14-1). For all four
264 experiments, the amount of H_2O loss was negligible (<0.1 wt%) near the interface and at the
265 center part of the glass where Cu diffusion profiles were measured. Therefore, measured
266 H_2O concentrations in the starting glasses (Table 1) were adopted as the H_2O concentrations
267 in the melt for all the experiments.
268
269 **RESULTS**

One example of the sample charge after an experiment is shown in Fig. 3a. The rhyolitic glasses show different optical features after the experiments. In general, synthetic hydrous glasses after low temperature experiments (Chal-Rhy-8-1, Chal-Rhy-11-1, Chal-Rhy-13-1) are opaque and slightly crystallized. Synthetic hydrous glasses after high temperature experiments (Chal-Rhy-3-1, Chal-Rhy-3-2, Chal-Rhy-7-1, Chal-Rhy-12-1, Chal-Rhy-14-1) show reddish color near the interface (e.g. Fig 4a, 4b). The reddish color in these glasses is caused by Cu-bearing nanoparticles in the glasses, as verified by high-magnification SEM images. These particles are too small in size (~75 nm in diameter) for their exact chemical composition to be quantified by SEM or EMP. Consistent diffusivities (within 20% difference) extracted from the time-series experiments (Chal-Rhy-3-1 and Chal-Rhy-3-2) that both contain Cu-bearing nanoparticles (Fig. 4a, 4b) suggest that these particles likely formed during quench. Because the analytical spot size is large, which averaged the nanoparticles in each spot, the nanoparticles do not affect the determination of diffusivities in our experiments. For all other experiments, the resulting glasses are transparent and colorless. An image of the sample charge after removing the chalcocite crystal is shown in Fig. 3b. Experimental conditions and results of all successful experiments are summarized in Table 3.

Absence of S diffusion profile

The original purpose of our experimental design was to obtain both Cu and S diffusivities in rhyolitic melts, as the dissolution of chalcocite (Cu_2S) would release Cu and S into the melt at an atomic ratio of 2:1. In addition, S diffusivity is lower than Cu diffusivity by a factor of 30 or more at the experimental temperatures, at least in basaltic melt (Ni and Zhang 2016). Hence, S concentration in the rhyolitic melt near the interface would be high and the difference between

interface S and far-field S concentrations would be easily measurable if chalcocite simply dissolved into the rhyolitic melt. Despite success in obtaining Cu diffusion profiles, however, we were unable to detect any S diffusion profile in the rhyolitic glass after the experiments. That is, S concentration variation in the rhyolitic glass is consistently below the detection limit of ±20 ppm. After careful examination of the experimental charge and by repeating the experiments, we recognized that the lack of S diffusion profile was not due to experimental errors, sample preparation, or the analysis. Instead, S stayed in the chalcocite phase at our experimental conditions. However, because:(i) S concentration in chalcocite is high, (ii) the chalcocite wafers used in the experiments are relatively large in size, and (iii) S diffusion distance in chalcocite can be significant, S concentration change in "chalcocite" after the experiments is small and is difficult to detect. In order to better understand the chemical reaction happening during the experiment, one experiment (Chal-Rhy-2-2) was specially conducted at 1096°C, in which we put a 15-μm-thick wafer of chalcocite sandwiched between two 1.5-mm-thick rhyolitic glass wafers (Fig. 5). The purpose of this experimental design was to use a small volume of chalcocite relative to rhyolitic glass, with which we might be able to detect a change in chalcocite composition. The composition of the chalcocite before the experiment was verified by EMP to be essentially pure chalcocite ($Cu_{1.96}Fe_{0.00}S$). After the experiment, the composition of run-product "chalcocite" has a composition of $Cu_{7.16}Fe_{0.27}S_4$, which roughly falls between the compositions of chalcocite (Cu_2S) and bornite (Cu_5FeS_4), as shown in Fig. 1. This result indicates that during the experiment, chalcocite lost Cu to and gained Fe from the surrounding rhyolitic melt, while S essentially remained in the sulfide phase. In addition to the change of chalcocite composition in Chal-Rhy-2-2, Cu and Fe diffusion profiles in the glass also agree with the loss of Cu to the melt and gain of Fe from the melt. Results of experiment Chal-Rhy-2-2 explain why a S diffusion profile was

316 not observed in the rhyolitic melt, and also show that our experiments are better characterized as
317 Cu-Fe exchange experiments between chalcocite and rhyolitic melt, rather than chalcocite
318 "dissolution" experiments.
319
320 **Cu diffusion profiles and fitting**
321 Typically three EMP traverses and one LA-ICP-MS traverse were analyzed perpendicular
322 to the interface to obtain the Cu concentration profiles in the separated glass wafer of each
323 sample. All EMP and LA-ICP-MS Cu diffusion profiles besides those in Fig. 4 are plotted in Fig.
324 6. The Cu concentrations measured using EMP are often somewhat higher than determined using
325 LA-ICP-MS (e.g., Chal-Ryh-1-2 in Fig. 6a), which is likely due to the imperfect choice of the
326 WDS background for EMP analyses. Near (within 45 μm) the interface, the Cu concentration
327 decreases toward the interface in the high-spatial-resolution EMP profile in Fig. 6a. This is
328 because during quench, Cu preferentially partitions into the chalcocite phase as temperature
329 decreases, leading to a Cu concentration decrease in the rhyolitic glasses near the interface.
330 Similar effects have been observed previously, typically within ~20 μm distance from the
331 mineral-melt interface (Zhang et al. 1989; Chen and Zhang 2008; Yu et al. 2016; Zhang and Xu
332 2016). LA-ICP-MS has lower spatial resolution, and only the first point close to the interface
333 might be affected by this decrease. The presence of this quench-affected profile indicates that a
334 negligible amount of melt is lost during separation of the chalcocite crystal (Zhang et al. 1989;
335 Chen and Zhang 2008; Yu et al. 2016). When fitting the profiles to obtain Cu diffusivities, the
336 portion of the profiles affected by quench was excluded. Assuming interface motion is negligible
337 because chalcocite is not dissolving (total Cu mass gained by the melt is less than that contained
338 in 1 μm chalcocite, meaning negligible interface motion anyway), the Cu concentration profiles

were fitted by the analytical solution to the one-dimensional diffusion in semi-infinite medium with constant interface concentration (Crank 1975) to obtain Cu diffusivities:

$$C = C_\infty + (C_0 - C_\infty)\,\mathrm{erfc}\frac{x}{2\sqrt{Dt}}, \quad (1)$$

where C_0 is the Cu concentration at the interface; C_∞ is the initial Cu concentration of the rhyolitic glass; x is the distance in the melt to the interface; D is Cu diffusivity and t is the experimental duration. Three parameters, C_0, C_∞ and D for each experiment, were obtained from curve fitting of the Cu concentration profile.

For experiment Chal-Rhy-3-1, which had the longest duration, it appears that diffusion reached the far-field boundary (Fig. 4a). Therefore, the Cu diffusion profile of Chal-Rhy-3-1 was fit with a different method, assuming a finite diffusion medium and an initial Cu concentration of 3.4 ppm (based on experiment Chal-Rhy-3-2, which used the same starting glass as Chal-Rhy-3-1).

Fitting results of all the experiments for both EMP and LA-ICP-MS results are summarized in Table 3. Although both EMP and LA-ICP-MS data were acquired for Cu diffusion profiles, Cu diffusivities fit from the LA-ICP-MS data were adopted for further discussion, while the high spatial resolution EMP data helped capture the short quench profile near the interface, and the multiple EMP traverses in each experiment helped to alleviate the concern of convection.

Fe diffusion profiles and fitting

Iron was observed to partition into the chalcocite during our experiments. Fe concentration profiles were measured by EMP to determine Fe diffusivities in the rhyolitic glasses (Fig. 7). Typically four traverses were analyzed by EMP perpendicular to the interface,

and the results are consistent with each other. Compared to the Cu diffusion profile in the same sample, the Fe diffusion profile is much shorter (e.g. Fig. 6a and Fig. 7a), which is consistent with the expectation that divalent Fe^{2+} diffuses at a much lower rate than monovalent Cu^{+} (Ni and Zhang 2016). Among the 15 experiments, resolvable Fe diffusion profiles were obtained in 8 experiments, as reported in Table 3. The remaining experiments either have an Fe diffusion profile that is too short (Chal-Rhy-4-2, Chal-Rhy-4-3 and Chal-Rhy-5-1) to be precisely analyzed, or exhibit anomalous behavior of Fe (experiment Chal-Rhy-8-1 has a flat Fe concentration profile in the rhyolitic glass; for Chal-Rhy-10-1, Fe concentration increases towards the interface). The anomalous behavior of Fe in experiments might be caused by the presence of bornite (Cu_5FeS_4) inclusions in the starting chalcocite. A small amount of bornite can greatly affect Fe activity in the chalcocite, but Cu activity would be affected to a much smaller degree. The Fe concentration profiles are fitted using Eq. (1), where the interface concentration (C_0) is lower than the far field concentration (C_∞) for Fe diffusion. All the fitted Fe diffusivities are reported in Table 3.

DISCUSSION

Possible convection

Because rhyolitic melts typically have high viscosities (~10^3 to 10^7 Pa·s at our experimental conditions according to the viscosity model by Hui and Zhang 2007), convection is unlikely a problem in our experiments. Nonetheless, two experiments (Chal-Rhy-3-1 and Chal-Rhy-3-2) were conducted with different durations of ~2 min and ~30 min to check for possible convection. The two experiments gave similar Cu diffusivities that are within 20% difference, implying no convection in our experiments (Fig. 4a, b). In addiction, multiple traverses were measured in

each experiment to verify that convection did not affect the diffusion profiles. Typically three EMP traverses ~200 μm away from each other were analyzed in each sample. Convection would lead to inconsistent profiles along different traverses, which is not the case for our experiments (Fig. 6). For LA-ICP-MS analysis, typically only one traverse was analyzed for each sample, but three LA-ICP-MS traverses ~300 μm away from each other were analyzed for the experiment at the highest temperature (Chal-Rhy-10-1). As can be seen in Fig. 6h, the concentration profiles observed along three traverses match almost perfectly with each other, indicating that convection was unlikely.

Sources of error

Uncertainty in temperature measurements is often an important source of error in diffusion studies. Because the activation energy of Cu diffusion is small, the error caused by temperature measurement uncertainties is within 10% for Cu diffusivities. Uncertainty in pressure measurement is also a negligible source of error, because based on our results, no obvious dependence of Cu diffusivity on pressure can be resolved from the 0.5 GPa and 1 GPa experiments.

Another source of error in our experiments is from diffusion during heating and quenching, especially because our shortest experimental duration is only ~2 min. Correction of the effective experimental duration was done using the solution to diffusion problems with a time-dependent diffusivity (Zhang 2008):

$$t_c = \frac{\int_0^t \exp(-E/RT)\,dt}{\exp(-E/RT_0)}, \quad (2)$$

where t_e is the effective experimental duration in seconds, T_0 is the target temperature in K, T is the recorded temperature corrected to the interface, and E is the activation energy of Cu diffusion. The above equation is theoretically rigorous for diffusion couple experiments, and the effect of heating (~50 s) and cooling (~10 s) is accounted for as equivalent duration at the target temperature. In this study, however, not only the diffusivity (D), but also the interface Cu concentration (C_0) in Eq. (1) is temperature dependent. Hence, an error might occur while using this correction method for our study. Because $\ln C_0$ for experiments in 4 wt% and 6 wt% H_2O rhyolitic melts is approximately linearly dependent on 1/T, the diffusion equation is numerically solved given the recorded temperature history with C_0 and D as a function of temperature. One example of the simulated profile is shown in Fig. 6j, where both the EMP profile and the LA-ICP-MS profile were modeled. As can be seen in the figure, the simulated profile fits the measured concentration profile well. In particular, the quench-affected part of the EMP profile is also well reproduced. After excluding the first ~40 μm of the modeled profiles, fitting the simulated "data" using Eq. (1) and effective duration from Eq. (2) recovers the input diffusivity within 5%. Therefore, effective experimental durations calculated using Eq. (2) are valid, and are shown in Table 3.

Dependence of Cu diffusivity on temperature, pressure and melt composition

All Cu diffusivities determined in this study are summarized on an Arrhenius plot in Fig. 8a, together with Cu diffusivities from previous studies as a comparison. Copper diffusivities obtained using Newberry Crater Obsidian (NCO) at 0.5 GPa and 1 GPa fall onto a single linear trend, indicating that the pressure dependence of Cu diffusion is insignificant. In order to examine the effect of major element composition on Cu diffusion, we compare Cu diffusion in

anhydrous silicate melts with different compositions. As can be seen in Fig. 8a, Cu diffusivities measured in two anhydrous rhyolitic glasses NCO (73.5 wt% SiO_2) and CIT (76.5 wt% SiO_2) by this study are in agreement within error. Copper diffusivity in anhydrous rhyolitic melts is about 0.5 natural logarithm units lower than in anhydrous basaltic melt (Ni and Zhang 2016) and about 0.5 natural logarithm units higher than in an anhydrous $Na_2Si_2O_5$ melt, in which Cu diffusivity was determined using a voltammetry method (von der Gonna and Russel 2000). Hence, Cu diffusivity in silicate melts is only weakly dependent on major element composition. The lower Cu^+ diffusivity in anhydrous $Na_2Si_2O_5$ melt with NBO/T = 1 than that in both anhydrous rhyolitic melt with NBO/T ≈ 0 and anhydrous Etna basalt with NBO/T ≈ 3/4 is somewhat unusual and may imply that Cu diffusivity determined using voltammetry is less reliable. Copper diffusivities calculated using the model by Mungall (2002) with a melt composition equivalent to NCO are also plotted in Fig. 8a for comparison. The calculated Cu diffusivities are a factor of 3 to 6 higher than our experimental data.

The concentration of H_2O in rhyolite has a stronger effect than major element compositions on Cu diffusivity. At 1000°C, every 2 wt% H_2O in the rhyolitic melt approximately doubles Cu diffusivity. Among monovalent elements, the effect of H_2O on Cu diffusion is greater than on Na (Zhang et al. 2010), but smaller than on Cs (Watson 1981). Fitting Cu diffusivities in anhydrous rhyolitic melts and rhyolitic melts containing 4 wt% and 6 wt% H_2O (Fig. 8a) give results as follows:

448 $$D_{Cu}^{anh} = \exp\left[-(14.52\pm0.49) - \frac{11950\pm699}{T}\right],\ r^2=0.9898 \quad (3a)$$

449 $$D_{Cu}^{4wt\%H_2O} = \exp\left[-(15.93\pm0.23) - \frac{8560\pm286}{T}\right],\ r^2=0.9989 \quad (3b)$$

450 $$D_{Cu}^{6wt\%H_2O} = \exp\left[-(16.15\pm0.39) - \frac{7439\pm438}{T}\right],\ r^2=0.9965, \quad (3c)$$

451

452 where diffusivities are in m^2/s, T is temperature in K, and errors are given in 1σ.

453 Fitting results show that, increasing H_2O content in rhyolitic melts not only increases Cu
454 diffusivity, but also decreases the activation energy. Activation energy of Cu diffusion in
455 anhydrous rhyolitic melts is 99.4±5.8 kJ/mol, decreasing to 71.2±2.4 kJ/mol in 4 wt% H_2O
456 rhyolitic melts and to 61.8±3.6 kJ/mol in 6 wt% H_2O rhyolitic melts. The decrease of activation
457 energy is approximately linear with increasing H_2O concentration in the rhyolitic glass (Fig. 8b).
458 Even in anhydrous rhyolitic melt, activation energy of Cu diffusion is small (~100 kJ/mol),
459 consistent with our expectation that Cu is diffusing as Cu^+ in the silicate melt.

460 If we consider H_2O concentration in the rhyolitic melt as an independent parameter, and
461 fit all Cu diffusivities by minimizing $\Sigma[(\ln D_{i,meas}-\ln D_{i,calc})/\sigma_i]^2$, where $\ln D_{i,meas}$, $\ln D_{i,calc}$ and σ_i are
462 the logarithm of measured diffusivity, that of calculated diffusivity and 1σ error for $\ln D_{i,meas}$,
463 respectively, we obtain the following expression of Cu diffusivity in rhyolitic melts containing
464 0.1 to 6 wt% water:

465 $$D_{Cu}^{Rhy} = \exp\left[-(14.75\pm0.35) - (0.23\pm0.10)w - \frac{(11647\pm491) - (698\pm117)w}{T}\right],\ r^2=0.9849 \quad (4)$$

466 where w is H_2O concentration in the rhyolitic melt in wt% and T is temperature in K. Eq. (4)
467 reproduces all of our Cu diffusivity data to within 0.19 natural logarithm units.

Because we now have Cu diffusion data in rhyolitic melts and basaltic melts (Ni and Zhang 2016), effort was made to model all Cu diffusion data in natural silicate melts. In order to incorporate melt composition as a factor in Cu diffusivity, mole percent of Si+Al on wet basis was first tried to fit the data. Previously, Yu et al. (2015) used the single compositional parameter of Si+Al to successfully model SiO_2 diffusivity in rhyolitic and anhydrous basaltic melts. Zhang and Xu (2016) were also able to use Si+Al to model Zr diffusivity in rhyolitic melts. Fitting our Cu diffusion data with Si+Al, however, does not reproduce the diffusivities in basaltic melts well. After some trials, we found that a single parameter of Si+Al-H can be used to account for melt composition in fitting Cu diffusivities in anhydrous basaltic melts and rhyolitic melts at 750°C to 1575 °C and 0.5 to 1.5 GPa:

$$D_{Cu} = \exp\left\{a + b(\text{Si+Al-H}) - \frac{c + d(\text{Si+Al-H})}{T}\right\}, \ r^2=0.9869 \quad (5)$$

with a=-17.3±0.9, b=3.8±1.5, c=4403±1094 and d=9700±1921. In Eq. (5) D_{Cu} is in m^2/s and T is temperature in K, and errors are given in 1σ. Eq. (5) reproduces Cu diffusivities in rhyolitic and basaltic melts (Ni and Zhang 2016) to within 0.35 natural logarithm units, with a 1σ standard deviation of 0.11 natural logarithm units. The success of using Si+Al-H instead of Si+Al in fitting Cu diffusivities indicates that the effect of H_2O in the melt on Cu diffusion is more than the simple dilution of network-forming cations as previously found for Zr diffusion (Zhang and Xu 2016) and Si diffusion (Yu et al. 2015). The difference in the compositional dependence of Cu diffusivity versus Si and Zr diffusivity may be attributed to the difference between the low-field strength ion Cu and high field strength ions Zr and Si.

As discussed earlier, the pressure effect on Cu diffusion is small. Incorporating pressure in the fitting yields a fitting error that is larger than the absolute value of the fitted parameter. In addition, applying Eq. (5) on Cu diffusivities in $Na_2Si_2O_5$ melt (von der Gonna and Russel 2000)

yields errors of up to 1.7 ln*D* units, meaning either our Cu diffusivity model does not apply to a melt composition of $Na_2Si_2O_5$, or Cu diffusivities obtained by the voltammetry method is less reliable, as discussed earlier.

Dependence of Fe diffusivities on temperature and H_2O concentration in rhyolitic melt

Iron diffusivities obtained in this study are summarized on an Arrhenius plot in Fig. 9. As can be seen in the figure, our Fe diffusivity data in anhydrous rhyolitic melt at 1 GPa approximate those reported in Baker and Watson (1988). Concentration of H_2O in the starting glass has a strong effect on Fe diffusivity. At 1050°C, every 1 wt% H_2O increases Fe diffusivity by a factor of ~3. Because not all the experiments yielded reliable Fe diffusivities, only in 4 wt% H_2O rhyolitic glasses produced enough data points to fit the Arrhenius equation:

$$D_{\mathrm{Fe}}^{4\mathrm{wt\%H_2O}} = \exp\left[-(14.45\pm0.66)-\frac{16845\pm809}{T}\right],\ r^2=0.9977 \quad (6)$$

where diffusivity is in m^2/s and T is temperature in K. The activation energy corresponding to Eq. (6) is 140.0±6.7 kJ. The above equation reproduces our experimental data to within 0.06 ln*D* units.

Combining our Fe diffusion data in anhydrous and hydrous rhyolite melts with data in Baker and Watson (1988), a general equation for Fe diffusivity in rhyolitic melts as a function of temperature and H_2O concentration is obtained as follows:

$$D_{Fe}^{Rhy} = \exp\left[-(16.1\pm1.7)-\frac{(19859\pm2541)-(1218\pm135)w}{T}\right],\ r^2=0.8359 \quad (7)$$

where diffusivity is in m^2/s and w is H_2O concentration in wt%. For the fitting of Eq. (7), because Fe diffusivities from Baker and Watson (1988) have larger errors (~0.25 natural logarithm units on average) than our data (~0.08 natural logarithm units), Cu diffusivities from

this study are weighted 9 times as important as the data from Baker and Watson (1988) to reflect the 3 times difference in error. The equation above corresponds to an activation energy of 165±21 kJ/mol for Fe diffusion in dry rhyolitic melts. Eq. (7) reproduces most data of this study and the study of Baker and Watson (1988) to less than 0.7 natural logarithm units, except for three data points in anhydrous rhyolitic melts, which are off by 0.9, 0.9 and 1.5 natural logarithm units respectively (Fig. 9).

For the diffusion of Fe, there is always concern as to whether Fe is diffusing as Fe^{2+} or Fe^{3+} in the experiments. As discussed in Zhang et al. (2010), Fe diffusion can be expressed as a linear combination of its Fe^{2+} and Fe^{3+} components:

$$D_{Fe} = X_{Fe^{2+}} D_{Fe^{2+}} + X_{Fe^{3+}} D_{Fe^{3+}} \quad (8)$$

where $X_{Fe^{2+}}$=Fe^{2+}/(Fe^{2+}+Fe^{3+}) and $X_{Fe^{3+}}$=Fe^{3+}/(Fe^{2+}+Fe^{3+}), respectively. Ferric iron has higher valence and is expected to diffuse at a much lower rate than Fe^{2+} in the melt. Therefore, the diffusion of Fe is usually due to the contribution of Fe^{2+}, as long as its relative abundance is high. Because our experimental durations are short, the oxidation state of Fe in the glass is likely controlled by the initial ferric/ferrous iron ratio. Rapid diffusion of H_2 or CO, however, can occur along the chalcocite-rhyolite interface and reduce Fe^{3+} in the rhyolitic glasses, thus increasing $X_{Fe^{2+}}$ values. One way to evaluate whether Fe^{2+} or Fe^{3+} is dominant in our experiments is to compare Fe diffusivities to Mg^{2+} diffusivities for a similar melt composition. This is because Fe^{2+} and Mg^{2+} are identical in valence and similar in size and hence are expected to have similar diffusivities. On the other hand, Fe^{3+} is trivalent and is expected to have significantly lower diffusivity than Mg^{2+}. As can be seen in Fig. 10, Fe diffusivities in anhydrous rhyolitic melts determined in this study are slightly higher than Mg^{2+} diffusivities in an anhydrous haplogranitic melt (Fig. 10), indicating that Fe diffusivities obtained in this study are mostly Fe^{2+} diffusivities.

536

537 **Comparison to diffusivities of other elements in rhyolitic melts**

538 Diffusivities of Cu and Fe are plotted in Fig. 10 to compare with other elements in
539 rhyolitic melts. According to Cu solubility and partitioning studies in basaltic, andesitic, and
540 rhyolitic melts (e.g., Ripley and Brophy 1995; Holzheid and Lodders 2001; Zajacz et al. 2012;
541 Zajacz et al. 2013; Liu et al. 2015), Cu dissolves into the silicate melt mostly as Cu^+ when
542 oxygen fugacity is below FMQ+4.4 (or NNO+3.6). Because oxygen fugacity in natural magmas
543 is usually within NNO±2 (Carmichael and Ghiorso 1990), and assuming that the valence state of
544 Cu does not change significantly with silicate melt composition, Cu should exist in most natural
545 magmas as Cu^+. Although the oxygen fugacity was not controlled during our experiments, the
546 use of graphite capsules provides a relatively reducing environment (below NNO based on
547 measured CO_2 concentrations in the melt; Holloway 1992), and it is expected that Cu is diffusing
548 as Cu^+ in our experiments. This conclusion is in accordance with the high diffusivity and low
549 activation energy of Cu based on our diffusion data. Comparison of Cu diffusivity to diffusivities
550 of alkali elements in anhydrous rhyolitic melt shows that, $D_{Li} \approx D_{Na} > D_{Cu} > D_K$, with D_{Cu}
551 approximately 1 order of magnitude smaller than D_{Li} and D_{Na}, and about 1 natural logarithm unit
552 higher than D_K (Fig. 10). According to Shannon (1976), in octahedral sites, Cu^+ has an ionic
553 radius of 0.77Å, similar to Li^+ (0.76 Å), smaller than Na^+ (1.02 Å), and significantly smaller than
554 K^+ (1.38 Å). These cations are compared at a fixed coordination number for self-consistency,
555 although they are not necessarily 6-coordinated in the silicate melt. The fact that Cu diffusivity is
556 larger than K diffusivity, but 1 order of magnitude smaller than that of Li and Na for anhydrous
557 rhyolitic melt means that monovalent cation diffusivity cannot be predicted based on ionic

558 radius. On the other hand, the activation energies for Cu, Li, Na and K in anhydrous rhyolitic
559 melts are similar. Their diffusivity trends are sub-parallel to each other, as can be seen in Fig. 10.

560 As shown in Fig. 10, Fe diffusivity in dry rhyolitic melt NCO is slightly higher than that
561 of Mg in a synthetic granitoid (HPG8) melt (Mungall et al. 1999), similar to that of Zn in the
562 same melt (Mungall et al. 1999), and much smaller than those of monovalent cations. The HPG8
563 melt, which contains 79.6 wt% SiO_2, is more silicic than NCO melt (73.5 wt% SiO_2), and hence
564 the lower Mg diffusivity in HPG8 relative to Fe diffusivity in NCO is probably largely due to the
565 bulk compositional differences. Diffusivity of Fe is about three orders of magnitude smaller than
566 Cu diffusivity, and about four orders of magnitude smaller than Li or Na diffusivity. The
567 activation energy of Fe diffusion is also significantly higher than Cu or alkali elements. This can
568 be seen in Fig. 10 from the steeper slope for Fe and Zn diffusivities than for the alkalis. In
569 addition, the effect of H_2O content on Fe diffusion is greater than on Cu diffusion. Iron
570 diffusivity in rhyolitic melt with 6 wt% H_2O is almost 4 orders of magnitude higher than that in
571 anhydrous rhyolitic melts (Fig. 9), whereas the difference between Cu diffusivities in 6 wt% H_2O
572 rhyolitic melt and anhydrous rhyolitic melts is only about 1 order of magnitude (Fig. 10). The
573 difference is consistent with literature data that demonstrate that dissolved H_2O typically has a
574 much stronger effect on the diffusivity of divalent cations than on monovalent cations in silicate
575 melts, or more generally, H_2O has a larger effect on elements with smaller diffusivities (Zhang et
576 al. 2010).

577 The new Cu^+ and Fe^{2+} diffusivities reported here allow us, to update the relative
578 diffusivity sequence of Zhang et al. (2010) in dry rhyolitic melts as follows:

579 $$Li \approx Na > Cu^+ > K > Ar \approx CO_2 \approx Cl \approx Rb \approx Sb \approx F > Ba \approx Cs \approx Sr > Ca > Fe^{2+} \approx S \approx Mg$$
580 $$> Be \approx B \approx Ta \approx Nb \approx Y \approx REE > Zr \approx U \approx Hf \approx Ti \approx Ge \approx Th \approx Si \approx P \quad (9)$$

In rhyolitic melts with 6 wt% H_2O, the sequence of diffusivities is:

$$Cu^{+} > H_2O > CO_2 > Cl > Fe^{2+} > S \quad (10)$$

At 1123 K, Cu diffusivity is ~50 times Cl diffusivity in anhydrous rhyolitic melts and ~30 times Cl diffusivity in rhyolitic melts with 6 wt% water. Also plotted in Fig. 10 are S diffusion data in 6 wt% H_2O rhyolitic melts from Baker and Rutherford (1996). Although the S diffusivities vary by almost two orders of magnitude over the temperature range 850 to 900 ºC, the data indicate that S diffusivity is much lower than Cl and Fe^{2+} diffusivity. Copper diffusivity is 4 to 5 orders of magnitude higher than S diffusivity in anhydrous rhyolitic melts and 6 wt% H_2O rhyolitic melt. One complication is that S diffusivities from Baker and Rutherford (1996) were obtained from anhydrite ($CaSO_4$) dissolution at an oxygen fugacity buffered by MNO, which is approximately FMQ+4.5 (O'Neill and Pownceby 1993). This indicates that S was diffusing in the form of S^{6+} or sulfate (SO_4^{2-}) in their experiments, instead of sulfide (S^{2-}) under the more reducing conditions typical of arc-related magmatic systems. Based on a study by Behrens and Stelling (2011), however, diffusivities of sulfide and sulfate are similar, at least in a soda lime (SiO_2-CaO-Na_2O) silicate melt. If diffusivities of sulfide and sulfate in natural silicate melt are also similar, our comparison of Cu and S diffusivities would not be affected by the diffusion species of S in silicate melts.

IMPLICATIONS

Prior to this study, the complete absence of experimental Cu diffusion data for rhyolitic melts required any assessment of Cu mobility in magmatic systems to use Cu diffusivities in an anhydrous $Na_2Si_2O_5$ melt (von der Gonna and Russel 2000) or theoretical values based on the model of Mungall (2002). Here, we use our new Cu diffusion data for rhyolite melts to assess the

604 transfer and partitioning behavior of Cu in an MVP-saturated magma. Our new Cu diffusion data
605 suggest that, in a fluid-saturated magma (melt + crystals + MVP) wherein Cu behaves
606 incompatibly in the fractionating crystal assemblage, the concentration of Cu in the MVP
607 exsolved from a hydrous rhyolitic melt would always be close to equilibrium partitioning,
608 because Cu diffusivity in the melt is higher than that of water and other elements (Fig. 10) (e.g.,
609 Zhang 2015). Experimental studies show that the Cu content of the MVP increases with
610 increasing Cl content of the MVP (Audetat and Simon 2012; Zajacz et al. 2012) wherein Cu is
611 complexed with Cl (i.e., CuCl; Candela and Holland 1984) or in the form of alkali-copper-
612 chloride complex (e.g., Na(/K)$CuCl_2$; Zajacz et al. 2011). Thus, the diffusion of Cl from the melt
613 to the MVP plays a key role not only in the Cl concentration in the MVP, but also in the
614 partitioning of Cu between the melt and the MVP. That is, once an MVP bubble forms, the
615 ability of the bubble to scavenge Cu depends on the Cl concentration in the MVP and hence the
616 diffusion of Cl from the melt to the MVP. The rapid diffusion of Cu would ensure that Cu
617 partitioning between the MVP and the melt is always approximately in equilibrium, whether the
618 MVP is made of individual bubbles or forms percolation clusters buoyantly rising through the
619 melt. Once Cl concentration in the MVP is modeled, the Cu concentration in the MVP can be
620 estimated from batch equilibrium partitioning. This conclusion is different from the modeling
621 results of Huber et al. (2012), mainly because a much lower Cu diffusivity (almost two orders of
622 magnitude lower than our experimental data) from von der Gonna and Russel (2000) was used in
623 their study.

624 Our Cu diffusion data can also be applied to elucidate the Cu and Zn isotope signatures of
625 tektites, such as in the studies of Moynier et al. (2009, 2010). These studies reported significant
626 depletion of both Cu (from typical upper crustal concentration of 28 ppm to ~2 ppm) and Zn

(from typical upper crustal concentration of 67 ppm to ~20 ppm) in tektites, where the typical upper crustal concentrations are from Rudnick and Gao (2014). In accordance with the depleted abundances of Zn and Cu, both metals exhibit enrichment of their heavy isotopes (+1.22‰ < $\delta^{66/64}$Zn < +2.49‰; +1.98‰ < $\delta^{65/63}$Cu < +6.99‰). To explain the more fractionated Cu isotope signature relative to Zn, Moynier et al. (2010) used the diffusion model of Mungall (2002) to estimate Cu^{+} diffusivity to be 2 orders of magnitude greater than Zn^{2+} diffusivity at 1150 ºC. Based on experimental data from this study and from Baker and Watson (1988), however, the difference is almost 4 orders of magnitude at 1150 ºC (Fig. 10). In general, our Cu diffusion data support the explanation by Moynier et al. (2010) that the more fractionated Cu isotope signature in tektites is likely due to the higher Cu diffusivity than Zn. It would be desirable to measure Cu and Zn concentration profiles in individual tektites to assess Cu and Zn loss, and to model the isotopic fractionation.

Acknowledgments: We thank J. C. Barrette for the assistance in LA-ICP-MS analysis, and Fabio Arzilli and James Mungall for their constructive and insightful reviews. P. Ni thanks Z. Xu for the training and help with FTIR analysis and piston-cylinder experiments. This work was partially supported by NSF grants EAR-1019440 and EAR-1524473 and NASA grant NNX15AH37G, and NSF grants EAR-1264560 and EAR-1250239 to ACS.

References:

Audetat, A., and Simon, A.C. (2012) Magmatic controls on porphyry Cu genesis. Geology and Genesis of Major Copper Deposits and Districts of the World: a Tribute to Richard Sillitoe. Society of Economic Geologists, Special Publication, 16, 553-572.

650 Bai T.B. and Koster van Groos, A.F. (1994) Diffusion of chlorine in granitic melts. Geochim
651 Cosmochim Acta, 58, 113-123.
652 Baker, L.L., and Rutherford, M.J. (1996) Sulfur diffusion in rhyolite melts. Contributions to
653 Mineralogy and Petrology, 123(4), 335-344.
654 Baker D.R., and Watson E.B. (1988) Diffusion of major and trace elements in compositionally
655 complex Cl- and F-bearing silicate melts. J Non-Cryst Solids, 102, 62-70
656 Behrens, H., and Stelling, J. (2011) Diffusion and redox reactions of sulfur in silicate
657 melts. Reviews in Mineralogy and Geochemistry, 73(1), 79-111.
658 Carmichael, I.S., and Ghiorso, M.S. (1990) The effect of oxygen fugacity on the redox state of
659 natural liquids and their crystallizing phases. Reviews in Mineralogy and
660 Geochemistry, 24(1), 191-212.
661 Candela, P.A., and Holland, H.D. (1984) The partitioning of copper and molybdenum between
662 silicate melts and aqueous fluids. Geochimica et Cosmochimica Acta, 48, 373-380.
663 Candela, P.A. (1991) Physics of aqueous phase evolution in plutonic environments. American
664 Mineralogist;(United States), 76.
665 Candela, P.A. (1997) A review of shallow, ore-related granites: textures, volatiles, and ore
666 metals. Journal of petrology, 38(12), 1619-1633.
667 Cassidy, W.A., Glass, B., and Heezen, B.C. (1969) Physical and chemical properties of
668 Australasian microtektites. Journal of Geophysical Research,74(4), 1008-1025.
669 Chen, Y., and Zhang, Y. (2008) Olivine dissolution in basaltic melt. Geochimica et
670 Cosmochimica Acta, 72(19), 4756-4777.
671 Crank, J. (1975) The Mathematics of Diffusion. Oxford, UK: Clarendon Press.
672 Fournelle, J.H., Kim, S., and Perepezko, J.H. (2005) Monte Carlo simulation of Nb Kα
673 secondary fluorescence in EPMA: comparison of PENELOPE simulations with experimental
674 results. Surface and interface analysis, 37(11), 1012-1016.
675 Harrison, T. M., and Watson, E.B. (1983) Kinetics of zircon dissolution and zirconium diffusion
676 in granitic melts of variable water content. Contributions to Mineralogy and Petrology, 84(1),
677 66-72.
678 Holloway, J. R., Pan, V., and Gudmundsson, G. (1992) High-pressure fluid-absent melting
679 experiments in the presence of graphite: oxygen fugacity, ferric/ferrous ratio and dissolved
680 CO_2. European Journal of Mineralogy, 4(1), 105-114.

681 Holzheid, A., and Lodders, K. (2001) Solubility of copper in silicate melts as function of oxygen
682 and sulfur fugacities, temperature, and silicate composition. Geochimica et Cosmochimica
683 Acta, 65(12), 1933-1951.
684 Huber, C., Bachmann, O., Vigneresse, J.L., Dufek, J., and Parmigiani, A. (2012) A physical
685 model for metal extraction and transport in shallow magmatic systems. Geochemistry,
686 Geophysics, Geosystems, 13(8).
687 Hui, H., and Zhang, Y. (2007) Toward a general viscosity equation for natural anhydrous and
688 hydrous silicate melts. Geochimica et Cosmochimica Acta, 71(2), 403-416.
689 Hui, H., Zhang, Y., Xu, Z., and Behrens, H. (2008) Pressure dependence of the speciation of
690 dissolved water in rhyolitic melts. Geochimica et Cosmochimica Acta, 72(13), 3229-3240.
691 Jambon A. (1982) Tracer diffusion in granitic melts: experimental results for Na, Rb, Cs, Ca, Sr,
692 Ba, Ce, Eu to 1300ºC and a model of calculation. J Geophys Res 87:10797-10810.
693 Jambon A., and Semet MP (1978) Lithium diffusion in silicate glasses of albite, orthoclase, and
694 obsidian compositions: an ion-microprobe determination. Earth Planet Sci Lett 37:445-450
695 Liu, X., Xiong, X., Audetat, A., and Li, Y. (2015) Partitioning of Cu between mafic minerals,
696 Fe–Ti oxides and intermediate to felsic melts. Geochimica et Cosmochimica Acta, 151, 86-
697 102.
698 Llovet, X., and Salvat, F. (2008) PENEPMA, A Monte Carlo code for the simulation of X-ray
699 emission spectra using PENELOPE.
700 Lodders, K. (2003) Solar system abundances and condensation temperatures of the
701 elements. The Astrophysical Journal, 591(2), 1220.
702 Moynier, F., Beck, P., Jourdan, F., Yin, Q.Z., Reimold, U., and Koeberl, C. (2009) Isotopic
703 fractionation of zinc in tektites. Earth and Planetary Science Letters, 277, 482-489.
704 Moynier, F., Koeberl, C., Beck, P., Jourdan, F., and Telouk, P. (2010) Isotopic fractionation of
705 Cu in tektites. Geochimica et Cosmochimica Acta, 74, 799-807.
706 Mungall, J.E., Dingwell, D.B., and Chaussidon, M. (1999) Chemical diffusivities of 18 trace
707 elements in granitoid melts. Geochimica et Cosmochimica Acta, 63(17), 2599-2610.
708 Mungall, J.E. (2002) Empirical models relating viscosity and tracer diffusion in magmatic
709 silicate melts. Geochimica et Cosmochimica Acta, 66, 125-143.
710 Newman, S., Stolper, E.M., and Epstein, S. (1986) Measurement of water in rhyolitic glasses--
711 calibration of an infrared spectroscopic technique. American Mineralogist, 71(11), 1527-41.

712 Ni, P., and Zhang, Y. (2016) Cu diffusion in a basaltic melt. American Mineralogist, 101(6),
713 1474-1482.
714 Ni, H., and Zhang, Y. (2008) H_2O diffusion models in rhyolitic melt with new high pressure
715 data. Chemical Geology, 250, 68-78.
716 O'Neill, H.S.C., and Pownceby, M.I. (1993) Thermodynamic data from redox reactions at high
717 temperatures. II. The MnO-Mn_3O_4 oxygen buffer, and implications for the thermodynamic
718 properties of MnO and Mn_3O_4.Contributions to Mineralogy and Petrology, 114(3), 315-320.
719 Parmigiani, A., Faroughi, S., Huber, C., Bachmann, O., and Su, Y. (2016) Bubble accumulation
720 and its role in the evolution of magma reservoirs in the upper crust. Nature, 532(7600), 492-
721 495.
722 Pearce, N.J., Perkins, W.T., Westgate, J.A., Gorton, M.P., Jackson, S.E., Neal, C.R., and
723 Chenery, S.P. (1997) A compilation of new and published major and trace element data for
724 NIST SRM 610 and NIST SRM 612 glass reference materials. Geostandards
725 newsletter, 21(1), 115-144.
726 Pettke, T., Oberli, F., Audétat, A., Guillong, M., Simon, A.C., Hanley, J.J., and Klemm, L.M.
727 (2012) Recent developments in element concentration and isotope ratio analysis of individual
728 fluid inclusions by laser ablation single and multiple collector ICP-MS. Ore Geology
729 Reviews, 44, 10-38.
730 Ripley, E.M., and Brophy, J.G. (1995) Solubility of copper in a sulfur-free mafic
731 melt. Geochimica et cosmochimica acta, 59(23), 5027-5030.
732 Rudnick, R.L., and Gao, S.X. (2014) Composition of the continental crust. Treatise on
733 geochemistry (Second Edition), 4, 1-51.
734 Shannon, R.T. (1976) Revised effective ionic radii and systematic studies of interatomic
735 distances in halides and chalcogenides. Acta Crystallographica Section A: Crystal Physics,
736 Diffraction, Theoretical and General Crystallography, 32(5), 751-767.
737 Simon, A.C., and Ripley, E.M. (2011). The role of magmatic sulfur in the formation of ore
738 deposits. Reviews in Mineralogy and Geochemistry, 73(1), 513-578.
739 Singer, D.A. (1995) World class base and precious metal deposits; a quantitative
740 analysis. Economic Geology, 90(1), 88-104.
741 von der Gonna, G., and Russel, C. (2000) Diffusivity of various polyvalent elements in a
742 $Na_2O\cdot 2SiO_2$ glass melt. Journal of non-crystalline solids, 261(1), 204-210.

743 Walter, L.S. (1967) Tektite compositional trends and experimental vapor fractionation of
744 silicates. Geochimica et Cosmochimica Acta, 31, 2043-2063.
745 Watson, E.B. (1981) Diffusion in magmas at depth in the Earth: The effects of pressure and
746 dissolved H_2O. Earth and Planetary Science Letters, 52(2), 291-301.
747 Wilkinson, J.J. (2013) Triggers for the formation of porphyry ore deposits in magmatic
748 arcs. Nature Geoscience, 6(11), 917-925.
749 Yang, Y., Zhang, Y., Simon, A.C., and Ni, P. (2016) Cassiterite dissolution and Sn diffusion in
750 silicate melts of variable water content. Chemical Geology, in revision.
751 Yu, Y., Zhang, Y., and Yang, Y. (2015) Diffusion of SiO_2 in rhyolitic melt. AGU Fall Meeting
752 abstract, submitted.
753 Yu, Y., Zhang, Y., Chen, Y., and Xu, Z. (2016) Kinetics of anorthite dissolution in basaltic
754 melt. Geochimica et Cosmochimica Acta, 179, 257-274.
755 Zajacz, Z., Seo, J.H., Candela, P.A., Piccoli, P.M., and Tossell, J.A. (2011) The solubility of
756 copper in high-temperature magmatic vapors: a quest for the significance of various chloride
757 and sulfide complexes. Geochimica et Cosmochimica Acta, 75(10), 2811-2827.
758 Zajacz, Z., Candela, P.A., Piccoli, P.M., Walle, M., and Sanchez-Valle, C. (2012) Gold and
759 copper in volatile saturated mafic to intermediate magmas: Solubilities, partitioning, and
760 implications for ore deposit formation. Geochimica et Cosmochimica Acta, 91, 140-159.
761 Zajacz, Z., Candela, P.A., Piccoli, P.M., Sanchez-Valle, C., and Walle, M. (2013) Solubility and
762 partitioning behavior of Au, Cu, Ag and reduced S in magmas. Geochimica et Cosmochimica
763 Acta, 112, 288-304.
764 Zhang, Y., Walker, D., and Lesher, C. E. (1989) Diffusive crystal dissolution. Contributions to
765 Mineralogy and Petrology, 102(4), 492-513.
766 Zhang, Y., Belcher, R., Ihinger, P.D., Wang, L., Xu, Z., and Newman, S. (1997) New calibration
767 of infrared measurement of dissolved water in rhyolitic glasses. Geochimica et
768 Cosmochimica Acta, 61(15), 3089-3100.
769 Zhang, Y. (2008) Geochemical kinetics. Princeton University Press.
770 Zhang, Y., Ni, H., and Chen, Y. (2010) Diffusion data in silicate melts. Reviews in Mineralogy
771 and Geochemistry, 72, 311-408.
772 Zhang, Y., and Xu, Z. (2016) Zircon saturation and Zr diffusion in rhyolitic melts, and zircon
773 growth geospeedometer. American Mineralogist, 101(6), 1252-1267.

774 Zhao, D., Zhang, Y., and Essene, E.J. (2015) Electron probe microanalysis and microscopy:
775 Principles and applications in characterization of mineral inclusions in chromite from
776 diamond deposit. Ore Geology Reviews, 65, 733-748.
777

778 **Figure captions**

779

780 **FIGURE 1**. Composition of chalcocite, bornite, and pure copper in the natural chalcocite cluster
781 and the "chalcocite" after experiment in Chal-Rhy-2-2 in the Cu-Fe-S ternary system (atomic
782 percent). Composition of the "chalcocite" after experiment (purple crosses) in Chal-Rhy-2-2
783 roughly falls in between chalcocite and bornite.

784

785

786 **FIGURE 2**. a) Apparent Cu concentration profiles due to secondary fluorescence, measured in
787 natural CIT glass next to a piece of chalcocite. Line 1 was measured from the contact to the far
788 field; Line 2 was measured when there is a tiny gap filled with epoxy between the chalcocite and
789 the glass; Line 3 was measured from the far field towards the contact; Line 4 was measured in
790 experimental charge Chal-Rhy-2-2, with a real Cu diffusion profile in the rhyolitic glass but
791 overwhelmed by the secondary fluorescence effect. b). Comparison of Monte Carlo simulated Cu
792 secondary fluorescence profile to electron microprobe measurements. The vertical axis is the raw
793 Cu Kα peak counts ratio on sample over Cu metal standard, without ZAF correction. An lx/lstd =
794 0.005 roughly corresponds to a Cu concentration of 0.6 wt%. In the simulation, the effect of the
795 orientation of the spectrometer is also examined: spectrometer 4 is oriented toward the chalcocite
796 side of the chalcocite-rhyolite couple, leading to higher Cu secondary fluorescence signals than
797 spectrometers 3 and 5.

798

799 **FIGURE 3**. a) Microscope image of a sample charge after piston cylinder experiment. The
800 chalcocite and the rhyolitic glass were naturally separated during quench probably because

rhyolitic melts do not wet on chalcocite. b) Microscope image of the same sample charge after double polishing, the removal of the chalcocite wafer, and analyses. Dark spots on the glass are laser ablation traverse spots and the red dashed lines show probe traverses for Cu concentration analysis.

FIGURE 4. Two experiments (forming a time series; one experiment in (a) and the other in (b)) to examine possible convection and the effect of Cu nanoparticles on Cu diffusivity extraction. The two experiments differ in duration by a factor of 12. Both products contain red Cu-bearing nanoparticles after the experiment. The Cu concentration profiles are plotted together with an image section of the sample glass to show correlations between the Cu concentration profile in the glass and existence of the Cu-bearing nanoparticles. The longer-duration experiment (Chal-Rhy-3-1) has a longer Cu diffusion profile, leading to the existence of Cu-bearing particles in a much wider region from the interface. Similar diffusivities (<20% different) obtained from these two experiments indicate that these particles had negligible effect on the diffusivities. a) Three EMP traverses and a traverse of LA-ICP-MS spots were analyzed for Chal-Rhy-3-1. The diffusivity provided in the figure is based on fitting result using the finite method. b) Sample Chal-Rhy-3-2 was measured by LA-ICP-MS only. The first point from the interface in open orange circle is likely affected by the short quench profile and is excluded from fitting.

FIGURE 5. Special experiment (Chal-Rhy-2-2) designed to examine the behavior of chalcocite during its "dissolution". "Dissolution" is in quotation marks because the reaction is better described as "metal exchange" instead of "dissolution". One thin wafer of chalcocite was sandwiched between two rhyolitic glasses in the experiment. The two rhyolitic glasses separated

824 during quench, and the gap was filled with epoxy for protection during polish. The chalcocite
825 was found containing 2.4 atom% Fe, 35.0 atom% S and 62.6 atom% Cu after the experiment,
826 indicating an exchange of Cu and Fe with the rhyolitic melts.

827

828 **FIGURE 6**. Copper diffusion profiles measured in this study (except for Chal-Rhy-3-1 and Chal-
829 Rhy-3-2, which are in Fig. 4). Solid symbols are LA-ICP-MS data (often one traverse only;
830 except for Chal-Rhy-10-1). Open orange circles indicate LA-ICP-MS data that are affected by
831 the quench effect and excluded from fitting. All other symbols are for EMP traverses (3 or more).
832 In j, the profiles are modeled considering the temperature effect on the interface Cu
833 concentration. Details about the modeling can be found in "sources of error".

834

835 **FIGURE 7**. Iron diffusion profiles obtained in this study that are used to extract Fe diffusivities in
836 Table 3. At least four electron microprobe traverses were analyzed perpendicular to the interface
837 for each sample. Fitting results for the experiments using Eq. (1) are also provided in the figures.

838

839 **FIGURE 8**. a) Arrhenius plot of all Cu diffusivities obtained in this study, together with those in
840 anhydrous basalt (Ni and Zhang 2016, at 0.5, 1 and 1.5 GPa), dry sodium silicate melt (von der
841 Gonna and Russel 2000, at 1bar) and calculated using the model of Mungall 2002 in NCO.
842 Experimental pressure is 0.5 GPa unless otherwise specified. Error bars reported for diffusivities
843 in natural silicate melts are all in 1σ (often smaller than the symbol). Diffusivities in anhydrous
844 rhyolite, 4wt% H_2O rhyolite and 6wt% H_2O rhyolite are fitted with linear functions respectively.
845 In general, Cu diffusivities show negligible dependence on pressure and weak dependence on

major element composition, but relatively strong dependence on H_2O concentration. b) Plot of activation energy versus concentration of H_2O in rhyolitic melts. Error bars are in 1σ. Increasing H_2O concentration in rhyolitic melts decreases the activation energy roughly linearly.

FIGURE 9. Iron diffusivities obtained in this study and from Baker and Watson 1988. All error bars shown are in 1σ. For some of the data points, error bars are smaller than the symbol size. Lines are calculated from the best-weighted fit of all data (Eq. 7).

FIGURE 10. Comparison of Cu diffusivities and Fe diffusivities to diffusivities of other elements in rhyolitic melts. Fitting of Fe diffusivities in anhydrous rhyolitic melt is adopted from Fig. 9. Data sources: Cu and Fe (anhydrous and 6 wt% H_2O rhyolitic melt, this study); Fe (anhydrous rhyolitic melt, diffusion couple method, P=1000 MPa, T= 1100 to 1400 ºC, Baker and Watson 1988); Li (anhydrous rhyolitic melt, tracer diffusivity, P=0.1 MPa, T=297 to 909 ºC, Jambon and Semet 1978); Na (anhydrous rhyolitic melt, P=0.1 MPa, extrapolated from T=138 to 502 ºC, Jambon 1982); K (anhydrous rhyolitic melt, P=0.1 MPa, T=372 to 845 ºC, Jambon 1982); Cs (anhydrous rhyolitic melt, P=100 MPa, T=602 to 915 ºC, Jambon 1982); H_2O_t (6wt% H_2O rhyolitic melt, Ni and Zhang 2008); Cl (anhydrous rhyolitic melt, P=0.1 to 100 MPa, T=850 to 1400 ºC, Bai and Koster van Groos 1994); Cl (6.9 wt% H_2O rhyolitic melt, P=100 and 200 MPa, T=850 ºC, Bai and Koster van Groos 1994); Zn (diffusion couple method, P=10 and 1000 MPa, T=898 to 1400 ºC, Baker and Watson 1988); Mg (synthetic granitoid melt HPG8, P=0.1 MPa, T=1137 to 1600 ºC, Mungall et al. 1999); S (anhydrite dissolution, anhydrous and 6.1 to 6.3 wt% H_2O rhyolitic melt, P=100 to 200 MPa, T=850 to 1100 ºC, MNO oxygen buffer, Baker and Rutherford 1996).

869

870 **TABLE 1**. Chemical composition of the rhyolitic glasses used for this study. Major element
871 compositions were measured by electron microprobe on starting glasses. Details for the EMP
872 analyses can be found in Analytical Methods. About 15 points were analyzed on each glass
873 sample and the average composition is reported below. All compositions are in wt%.

	SiO_2	TiO_2	Al_2O_3	FeO_t	MgO	CaO	Na_2O	K_2O	H_2O^*	Total
NCO	73.45	0.23	14.04	2.00	0.14	0.75	5.35	4.30	0.10	100.36
CIT	76.51	0.05	12.48	1.02	0.02	0.41	4.32	4.92	0.24	99.97
bb7b-25	75.26	0.06	12.26	1.05	0.02	0.52	3.96	4.85	1.80	99.78
GMR+2	72.07	0.26	13.41	1.65	0.27	1.22	4.12	4.44	1.99	99.43
GMR+4	70.53	0.26	13.16	1.71	0.27	1.20	4.03	4.35	3.89	99.40
GMR+6	69.22	0.25	12.94	1.66	0.27	1.17	3.90	4.20	5.95	99.56

874 *Concentration of H_2O was measured by FTIR, each value is the average of ~10 analysis on the same sample.
875

876 **TABLE 2**. Instrumental parameters and operating conditions of the LA-ICP-MS

Laser-ablation system	
Laser system	PhotonMachines 193 nm short pulse width Analyte Excite excimer laser ablation system
Energy	6.33 J/cm^2
Spot size	25 µm
Pulse rate	25 Hz
Carrier gas flow	1.2 L/min (He)
ICP-MS system	
Instrument model	Agilent 7900
RF power	1250 W
Auxiliary gas flow rate	0 L/min (no make up or dilute gas used)
Nebulizer gas flow rate	0.8 L/min (Ar)
Interface cones	Agilent Ni Sampler cone #G3280-67040
	Agilent Ni Skimmer cone #G3280-67041
Dwell time	10 ms on ^{43}Ca, ^{44}Ca, ^{57}Fe, ^{63}Cu and ^{65}Cu
Background	30 s

877

This is a preprint, the final version is subject to change, of the American Mineralogist (MSA)
Cite as Authors (Year) Title. American Mineralogist, in press.
(DOI will not work until issue is live.) DOI: http://dx.doi.org/10.2138/am-2017-5885

878 **TABLE 3**. Summary of experimental conditions and results.

Exp#	*P* (GPa)	*T* (ºC)	Starting glass	Duration (s)		D_{Cu} ($\times10^{-12}m^2/s$)		D_{Fe} ($\times10^{-12}m^2/s$)
				t_1 (s)	t_2(s)	EMP	ICP-MS	
Chal-Rhy-1-2	0.5	1101	bb7b-25	428.9	464.8	113.0±8.1	**126.1±5.8**	0.185±0.011
Chal-Rhy-2-2*	0.5	1096	GMR+2	n.a.	n.a.	n.a.	**n.a.**	n.a.
Chal-Rhy-3-1**	0.5	1001	GMR+2	1804.4	1830.8	n.a.	**95.5±3.6**	0.166±0.005
Chal-Rhy-3-2	0.5	1003	GMR+2	118.9	146.7	n.a.	**80.7±1.5**	n.a.
Chal-Rhy-4-2	0.5	1099	CIT	909.9	932.9	56±13	**92.8±3.9**	–
Chal-Rhy-4-3	0.5	1088	NCO	906.8	936.1	69±14	**80.2±5.5**	–
Chal-Rhy-5-1	0.5	1006	NCO	902.8	930.2	50±14	**38.6±2.0**	–
Chal-Rhy-7-1	0.5	941	GMR+6	244.7	286.7	277±45	**215.6±6.1**	2.39±0.21
Chal-Rhy-8-1	0.5	750	GMR+6	231.9	279.4	36.2±6.6	**68.1±0.9**	–
Chal-Rhy-9-1	1	1303	NCO	120.8	148.7	223±14	**241.4±4.3**	0.273±0.028
Chal-Rhy-10-1	1	1391	NCO	118.9	153.4	483±20	**372.5±6.6**	1.75±0.11
Chal-Rhy-11-1	0.5	854	GMR+6	246.4	284.3	157±15	**126.6±1.4**	–
Chal-Rhy-12-1	0.5	954	GMR+4	239.3	270.2	97.4±6.6	**110.1±3.4**	0.548±0.025
Chal-Rhy-13-1	0.5	856	GMR+4	247.4	279.4	76±13	**61.9±2.1**	0.195±0.033
Chal-Rhy-14-1	0.5	1049	GMR+4	120.1	152.7	195.7±7.5	**187.5±6.0**	1.482±0.073

879 *Note: P* is corrected pressure; *T* is corrected interface temperature; t_1 is recorded duration at target temperature ±1 ºC;
880 t_2 is effective duration calculated using Eq. (2). All reported errors are at 1σ level.
881 *Experiment Chal-Rhy-2-2 was specially designed to study the composition change of chalcocite crystal during
882 experiment. Therefore no diffusivities were determined for the experiment.
883 **Copper diffusivity in Chal-Rhy-3-1 was fit assuming diffusion in finite medium using the same initial Cu
884 concentration as Chal-Rhy-3-2.

This is a preprint, the final version is subject to change, of the American Mineralogist (MSA)
Cite as Authors (Year) Title. American Mineralogist, in press.
(DOI will not work until issue is live.) DOI: http://dx.doi.org/10.2138/am-2017-5885

Fig.1

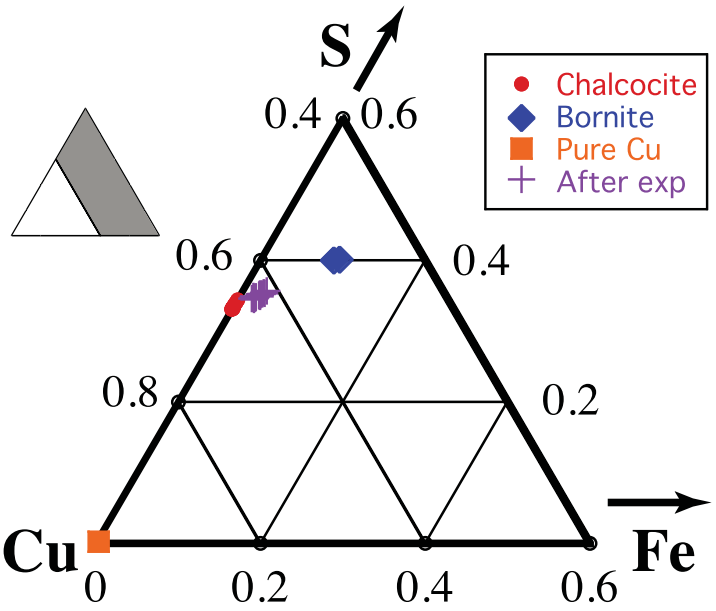

This is a preprint, the final version is subject to change, of the American Mineralogist (MSA)
Cite as Authors (Year) Title. American Mineralogist, in press.
(DOI will not work until issue is live.) DOI: http://dx.doi.org/10.2138/am-2017-5885

Fig.2a

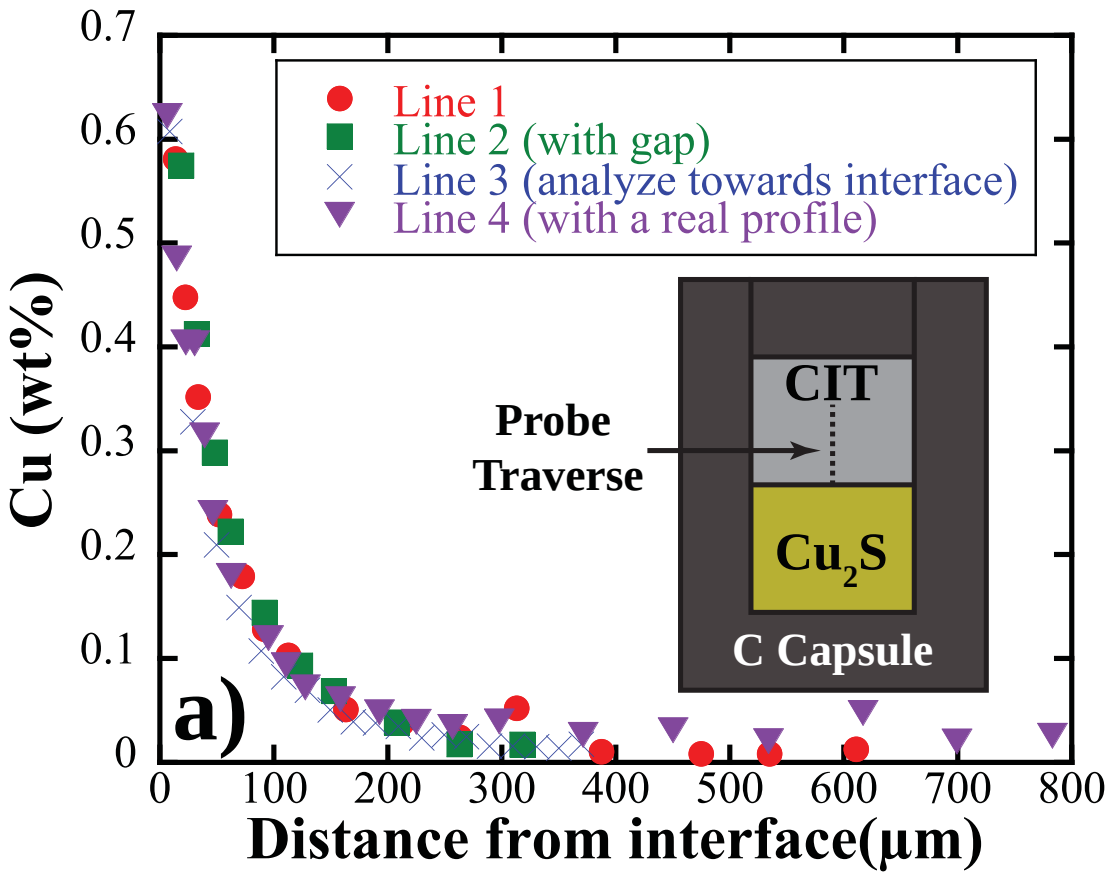

This is a preprint, the final version is subject to change, of the American Mineralogist (MSA)
Cite as Authors (Year) Title. American Mineralogist, in press.
(DOI will not work until issue is live.) DOI: http://dx.doi.org/10.2138/am-2017-5885

Fig.2b

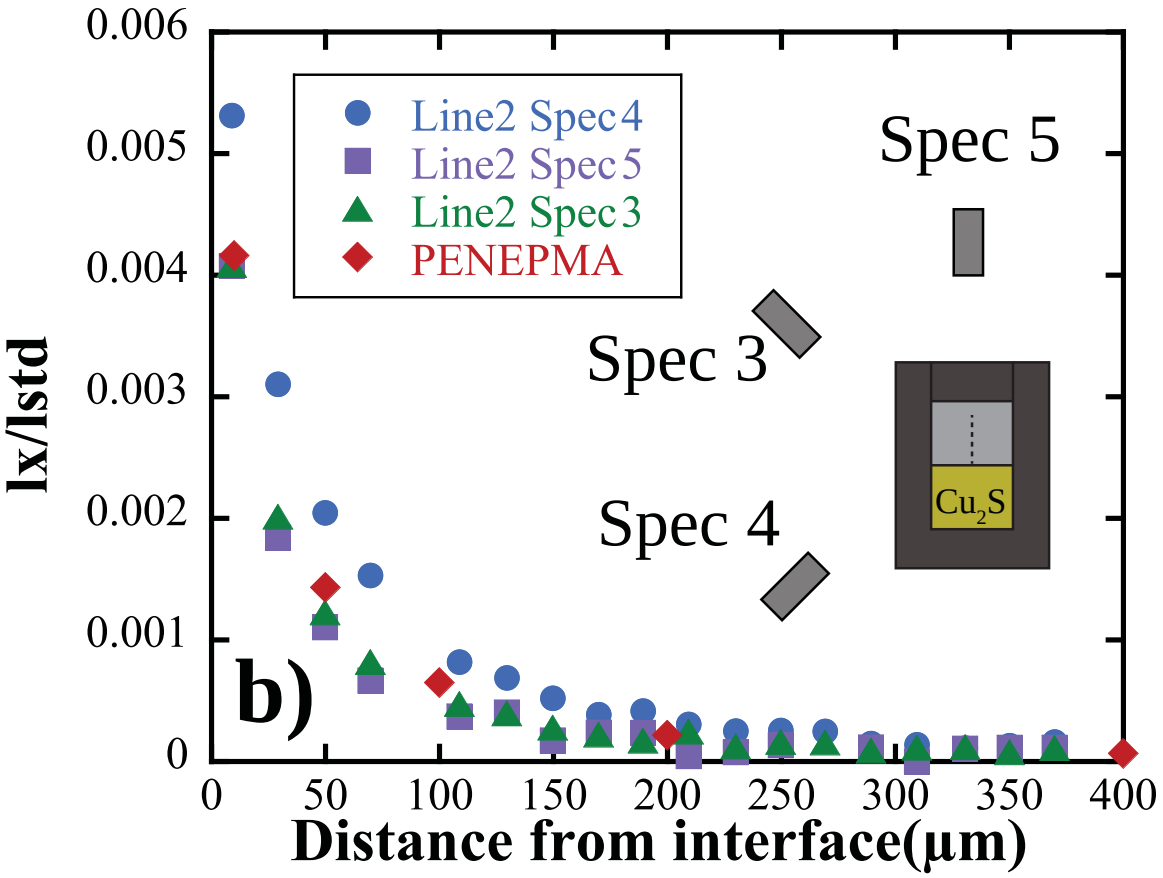

This is a preprint, the final version is subject to change, of the American Mineralogist (MSA)
Cite as Authors (Year) Title. American Mineralogist, in press.
(DOI will not work until issue is live.) DOI: http://dx.doi.org/10.2138/am-2017-5885

Fig.3a

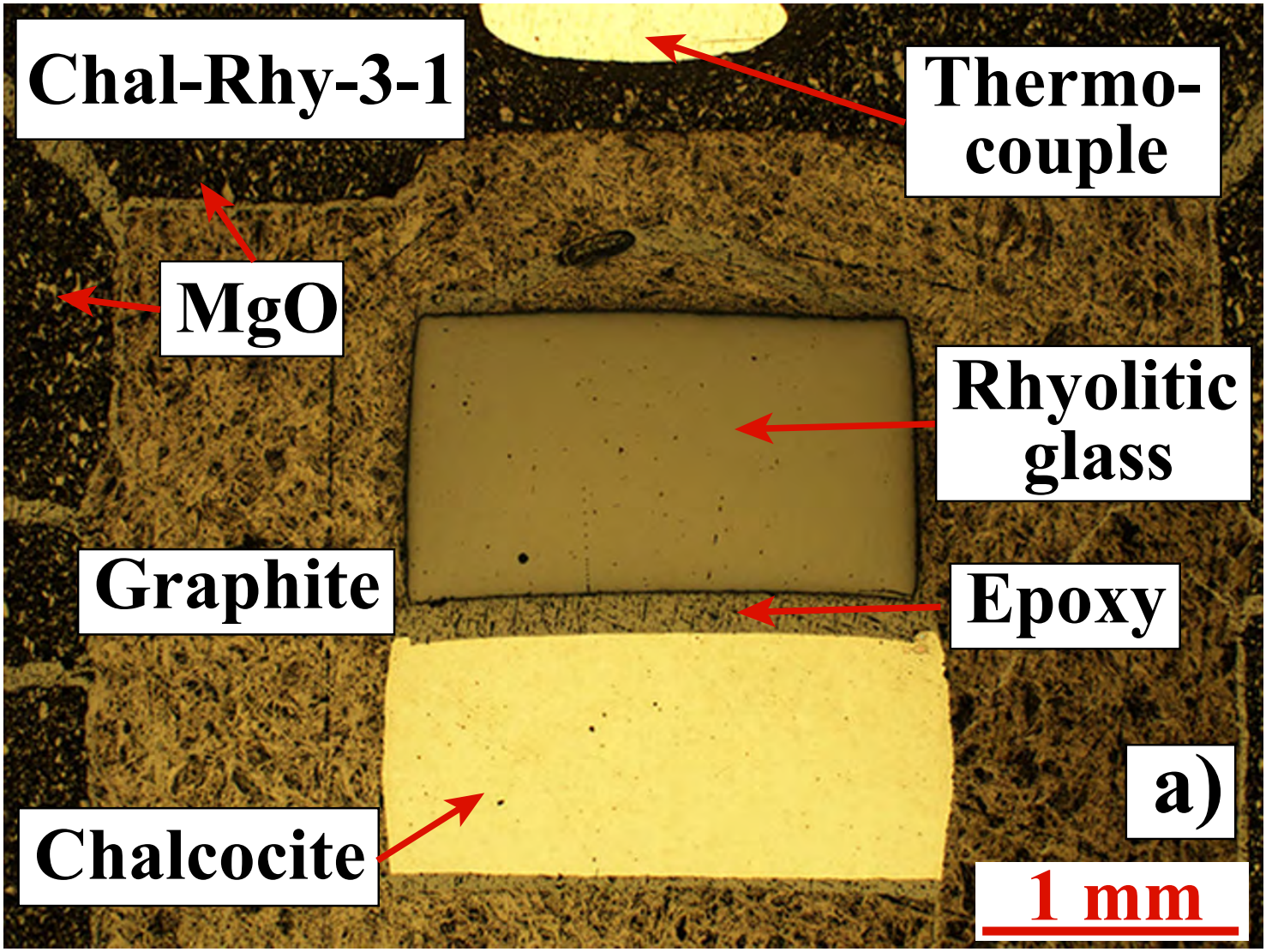

This is a preprint, the final version is subject to change, of the American Mineralogist (MSA)
Cite as Authors (Year) Title. American Mineralogist, in press.
(DOI will not work until issue is live.) DOI: http://dx.doi.org/10.2138/am-2017-5885

Fig.3b

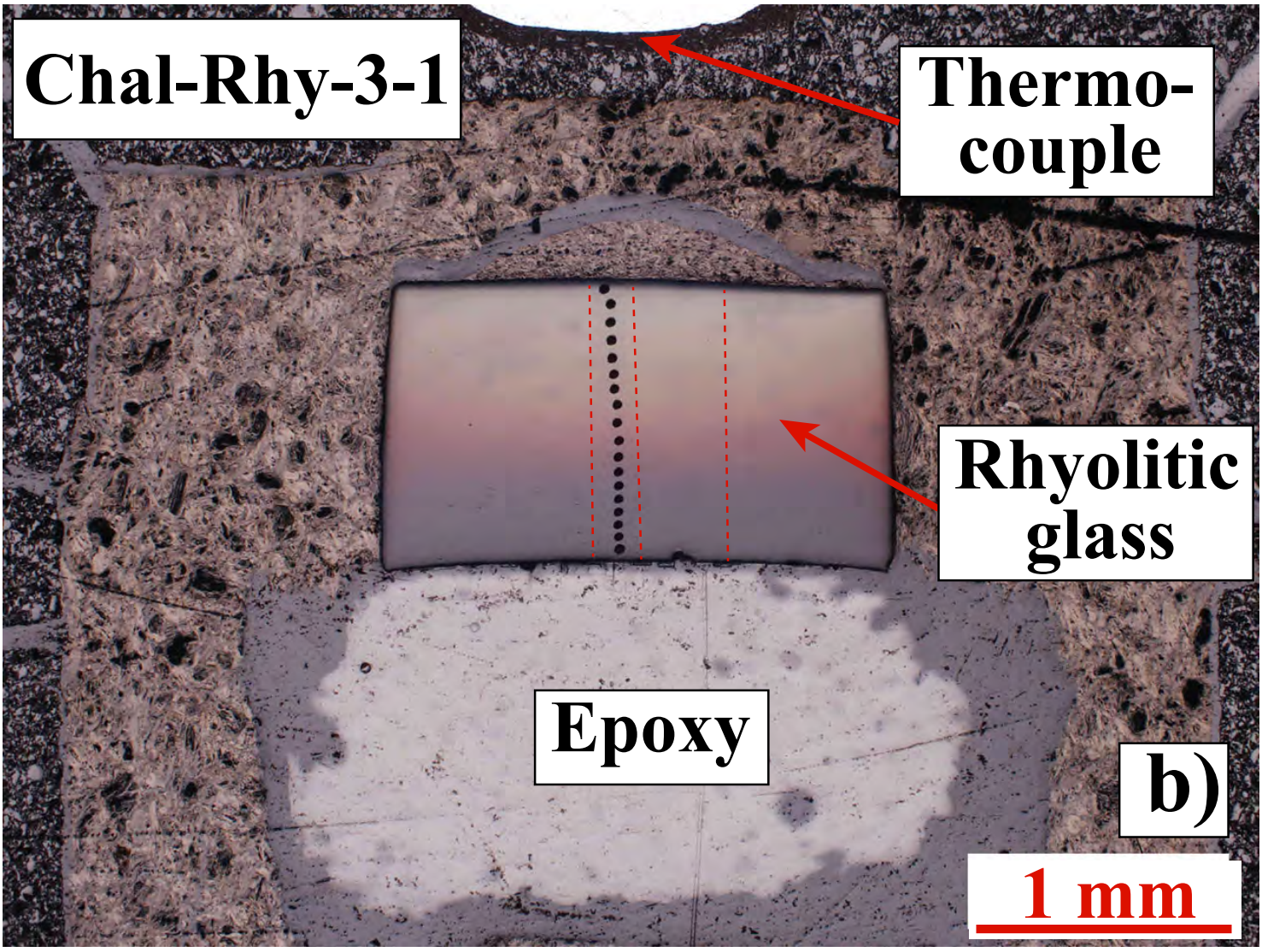

This is a preprint, the final version is subject to change, of the American Mineralogist (MSA)
Cite as Authors (Year) Title. American Mineralogist, in press.
(DOI will not work until issue is live.) DOI: http://dx.doi.org/10.2138/am-2017-5885

Fig.4a

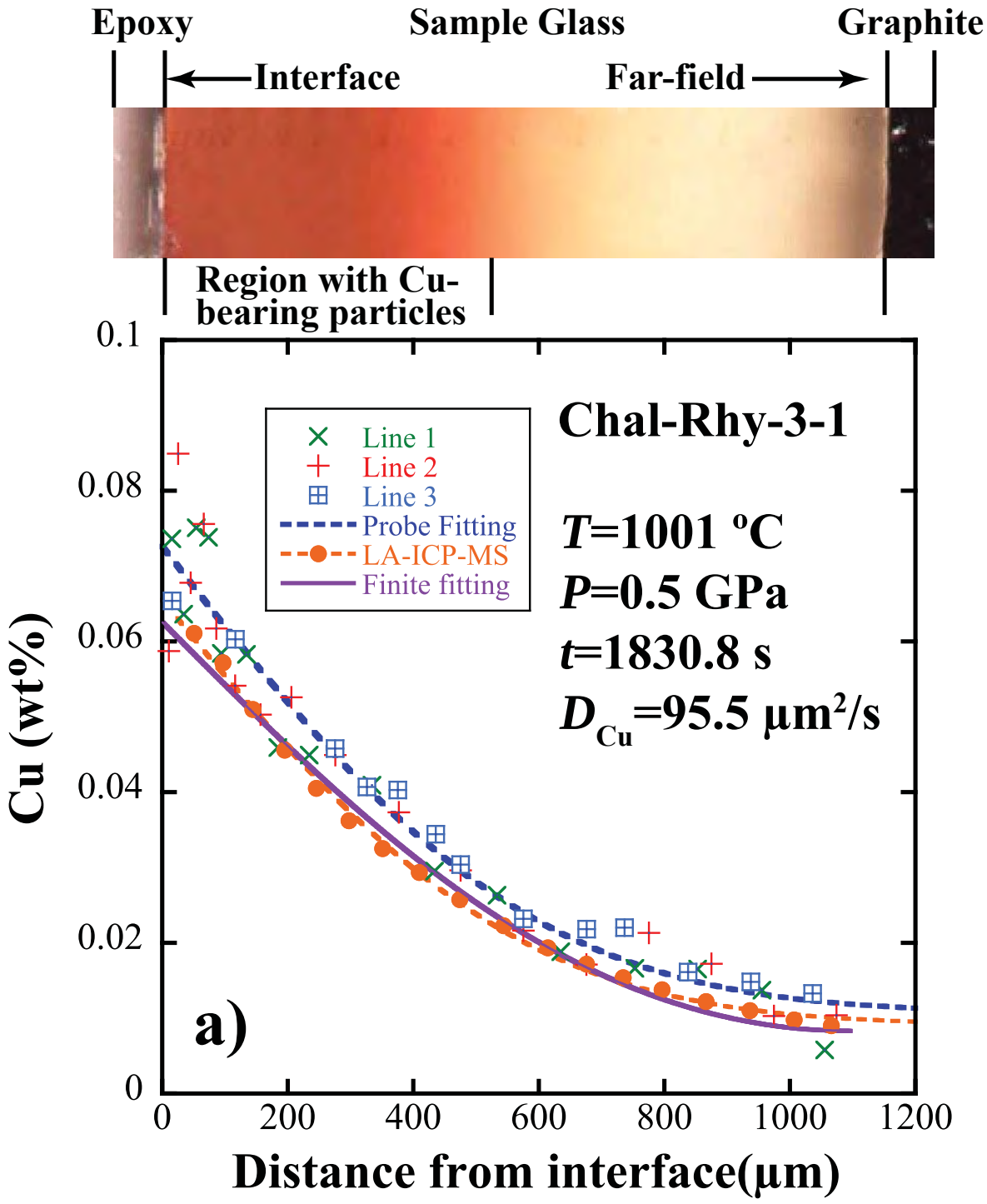

This is a preprint, the final version is subject to change, of the American Mineralogist (MSA)
Cite as Authors (Year) Title. American Mineralogist, in press.
(DOI will not work until issue is live.) DOI: http://dx.doi.org/10.2138/am-2017-5885

Fig.4b

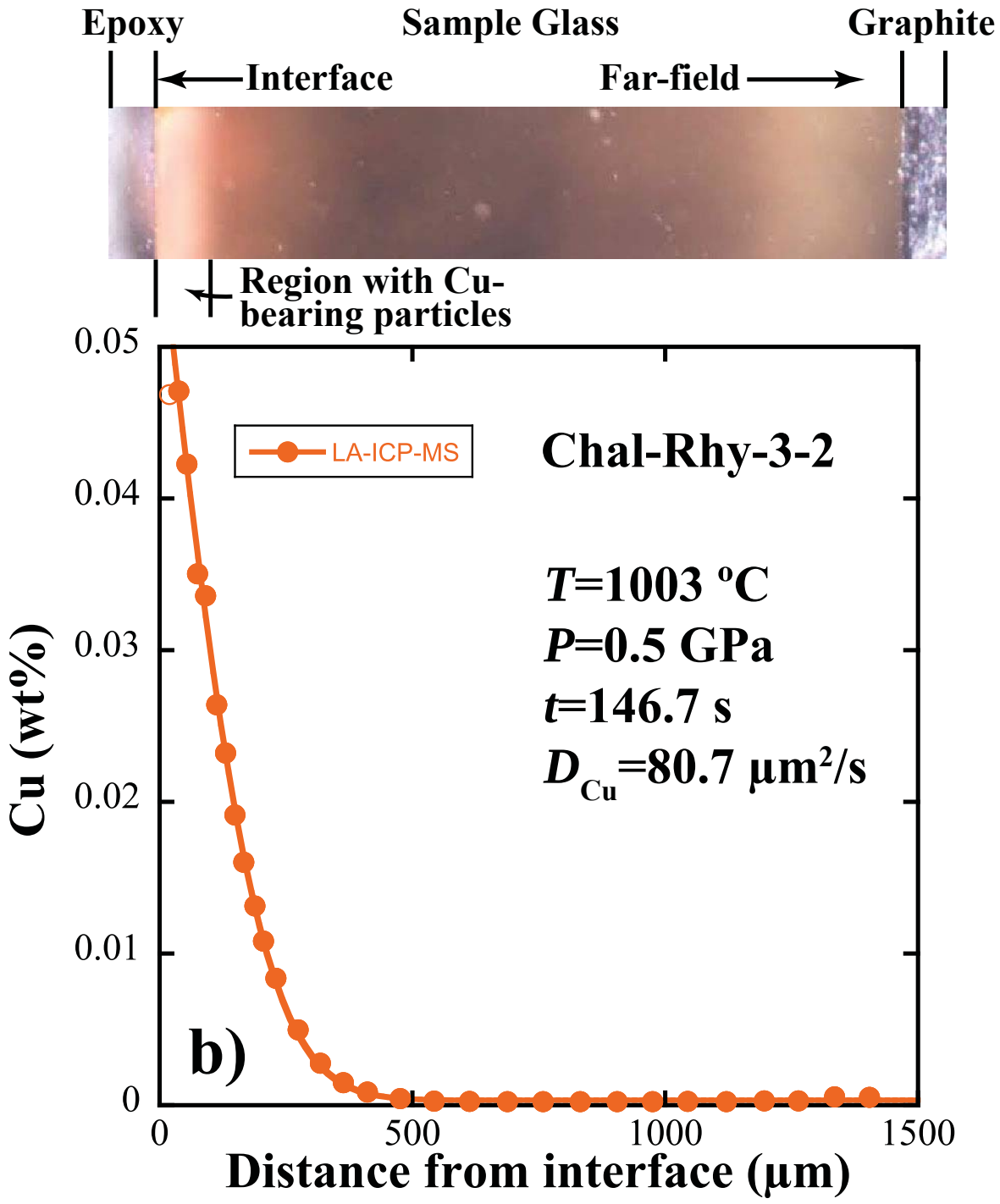

This is a preprint, the final version is subject to change, of the American Mineralogist (MSA)
Cite as Authors (Year) Title. American Mineralogist, in press.
(DOI will not work until issue is live.) DOI: http://dx.doi.org/10.2138/am-2017-5885

Fig.5

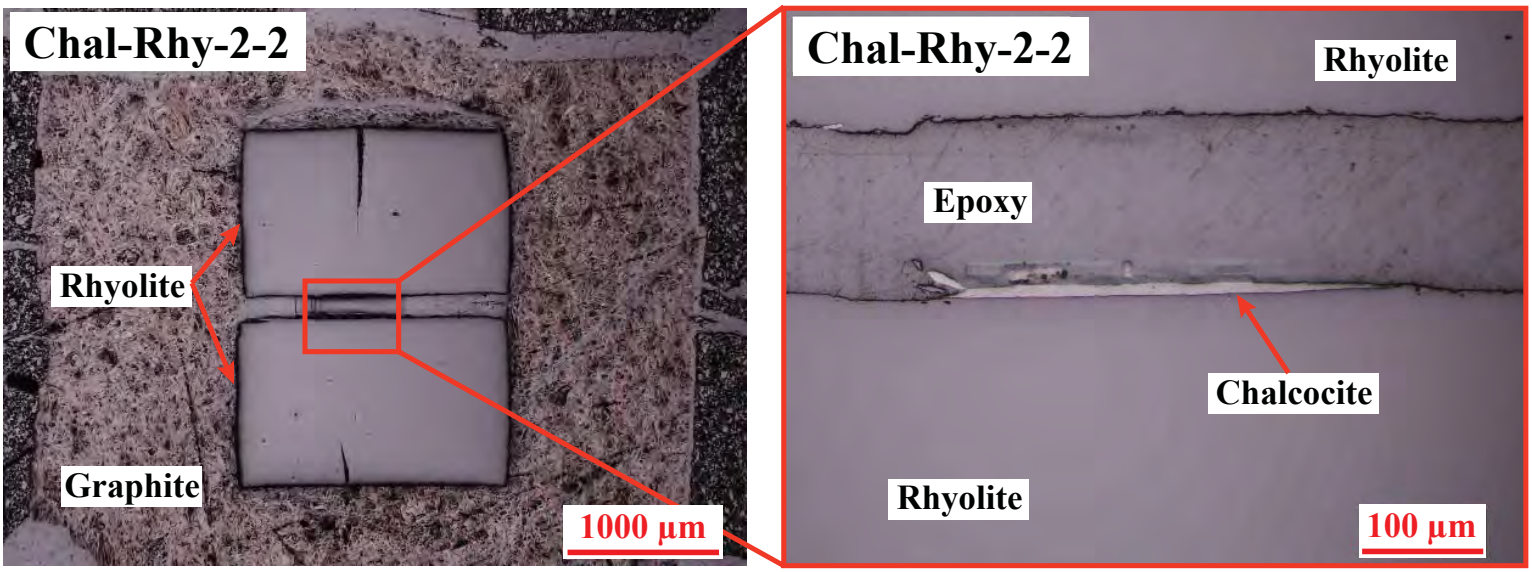

This is a preprint, the final version is subject to change, of the American Mineralogist (MSA)
Cite as Authors (Year) Title. American Mineralogist, in press.
(DOI will not work until issue is live.) DOI: http://dx.doi.org/10.2138/am-2017-5885

Fig.6a

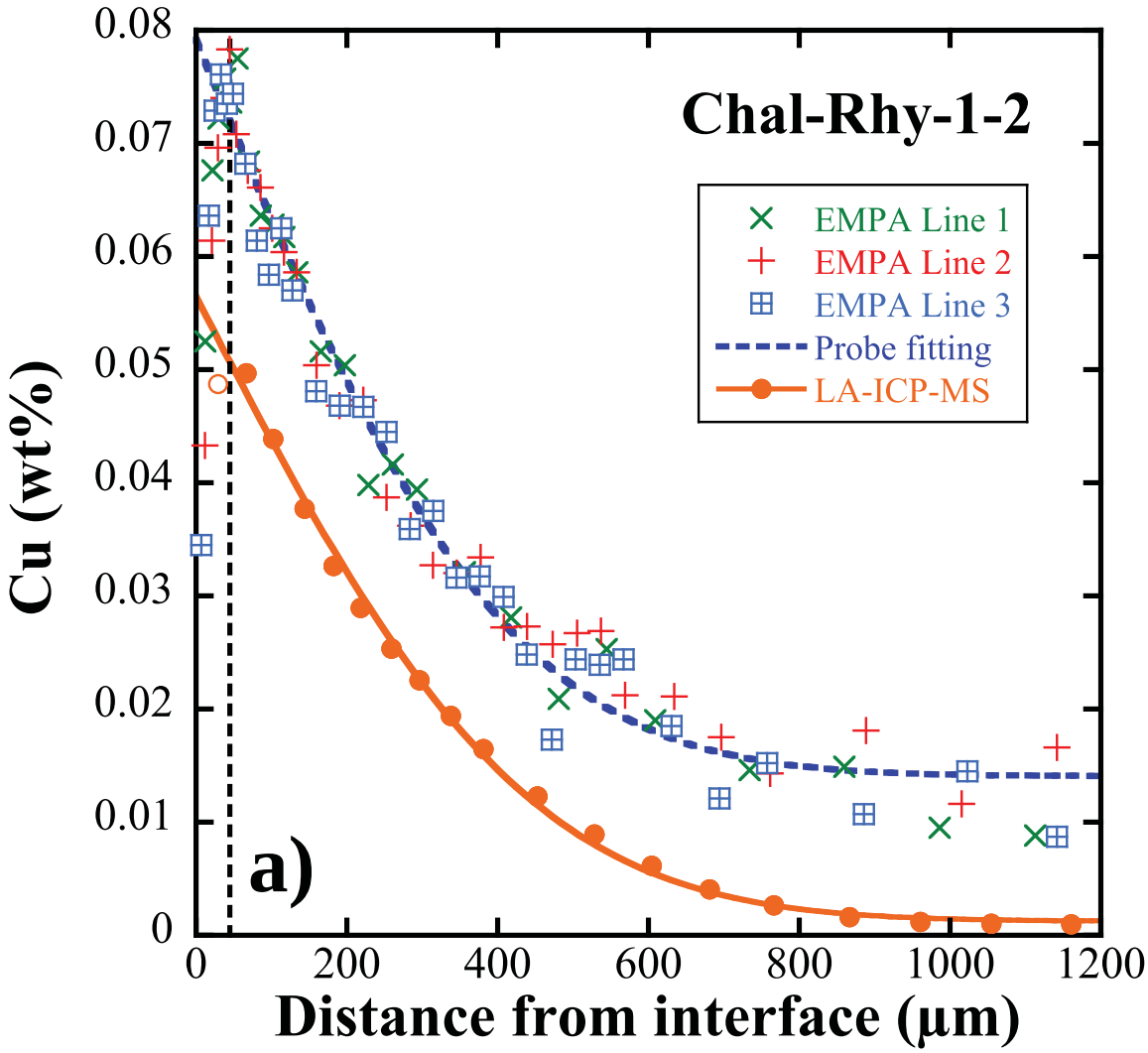

This is a preprint, the final version is subject to change, of the American Mineralogist (MSA)
Cite as Authors (Year) Title. American Mineralogist, in press.
(DOI will not work until issue is live.) DOI: http://dx.doi.org/10.2138/am-2017-5885

Fig.6b

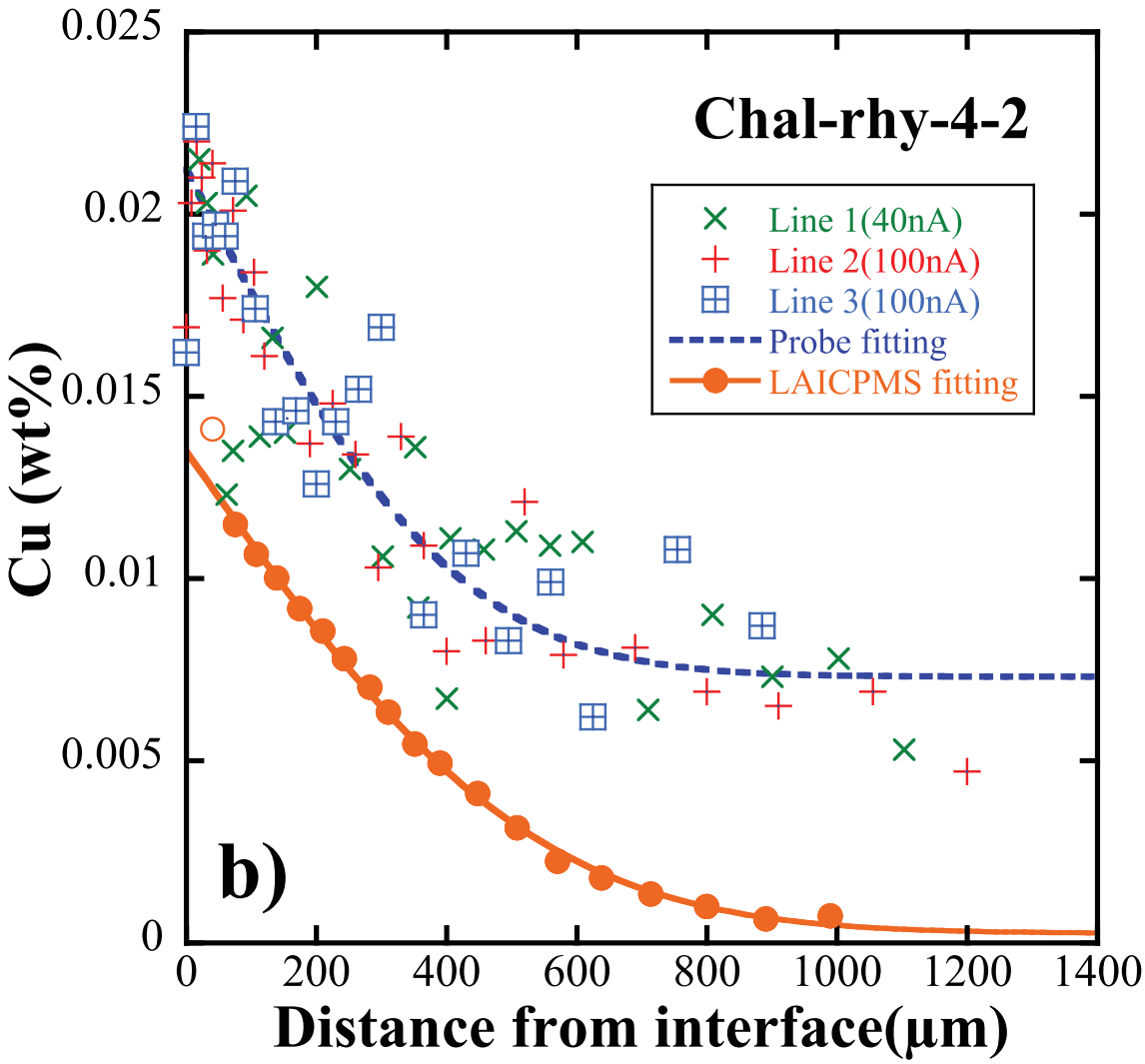

This is a preprint, the final version is subject to change, of the American Mineralogist (MSA)
Cite as Authors (Year) Title. American Mineralogist, in press.
(DOI will not work until issue is live.) DOI: http://dx.doi.org/10.2138/am-2017-5885

Fig.6c

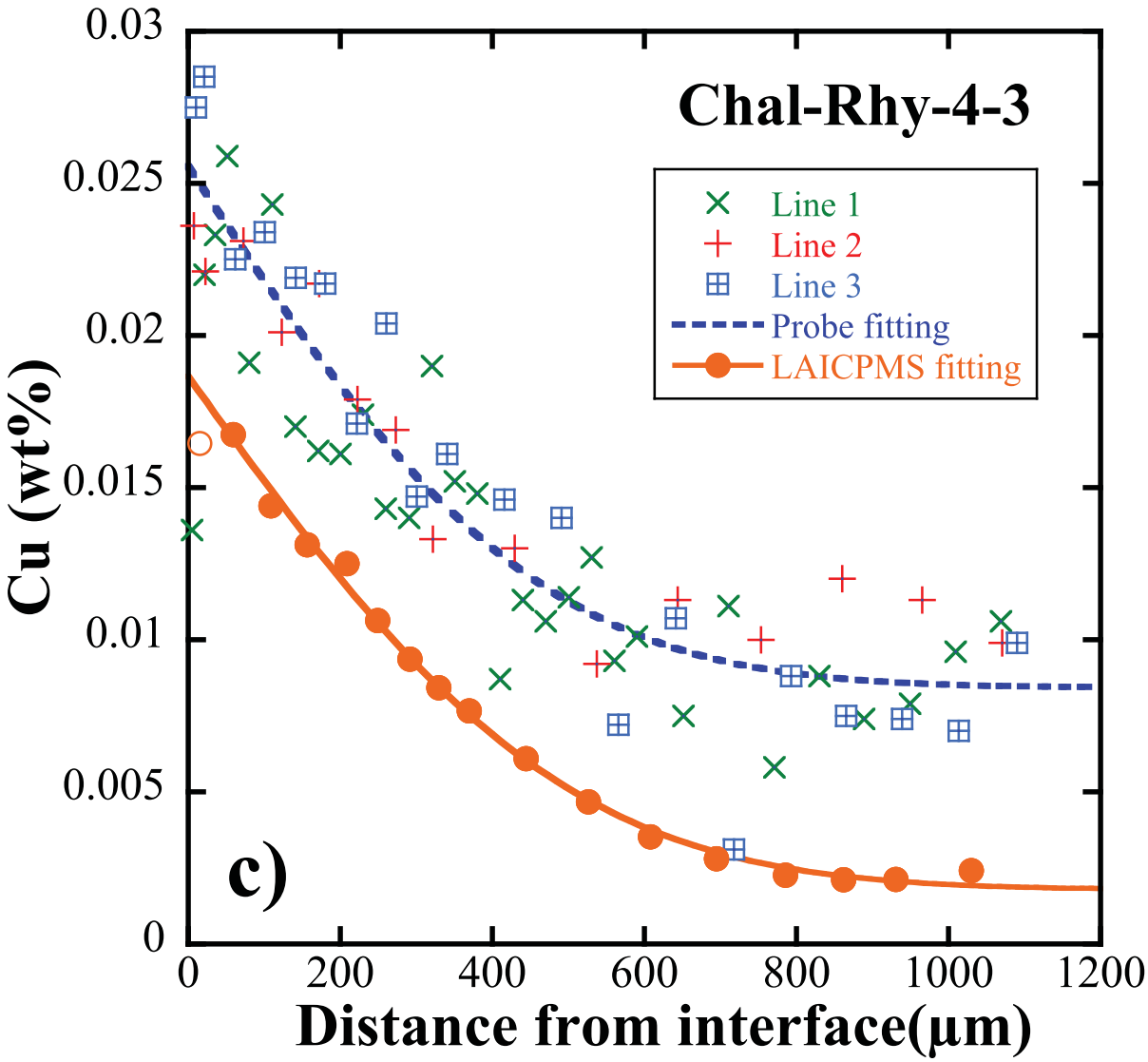

This is a preprint, the final version is subject to change, of the American Mineralogist (MSA)
Cite as Authors (Year) Title. American Mineralogist, in press.
(DOI will not work until issue is live.) DOI: http://dx.doi.org/10.2138/am-2017-5885

Fig.6d

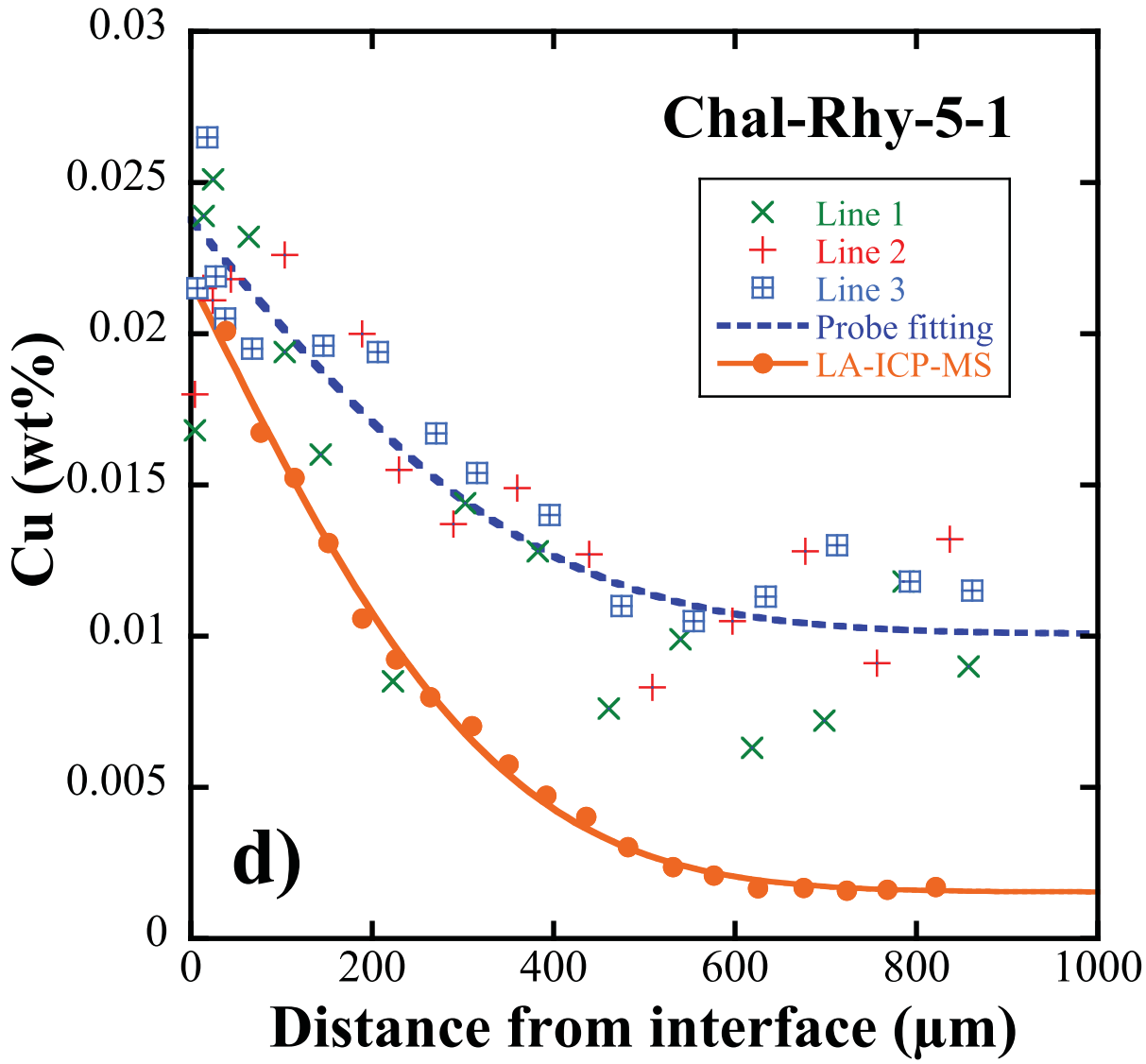

This is a preprint, the final version is subject to change, of the American Mineralogist (MSA)
Cite as Authors (Year) Title. American Mineralogist, in press.
(DOI will not work until issue is live.) DOI: http://dx.doi.org/10.2138/am-2017-5885

Fig.6e

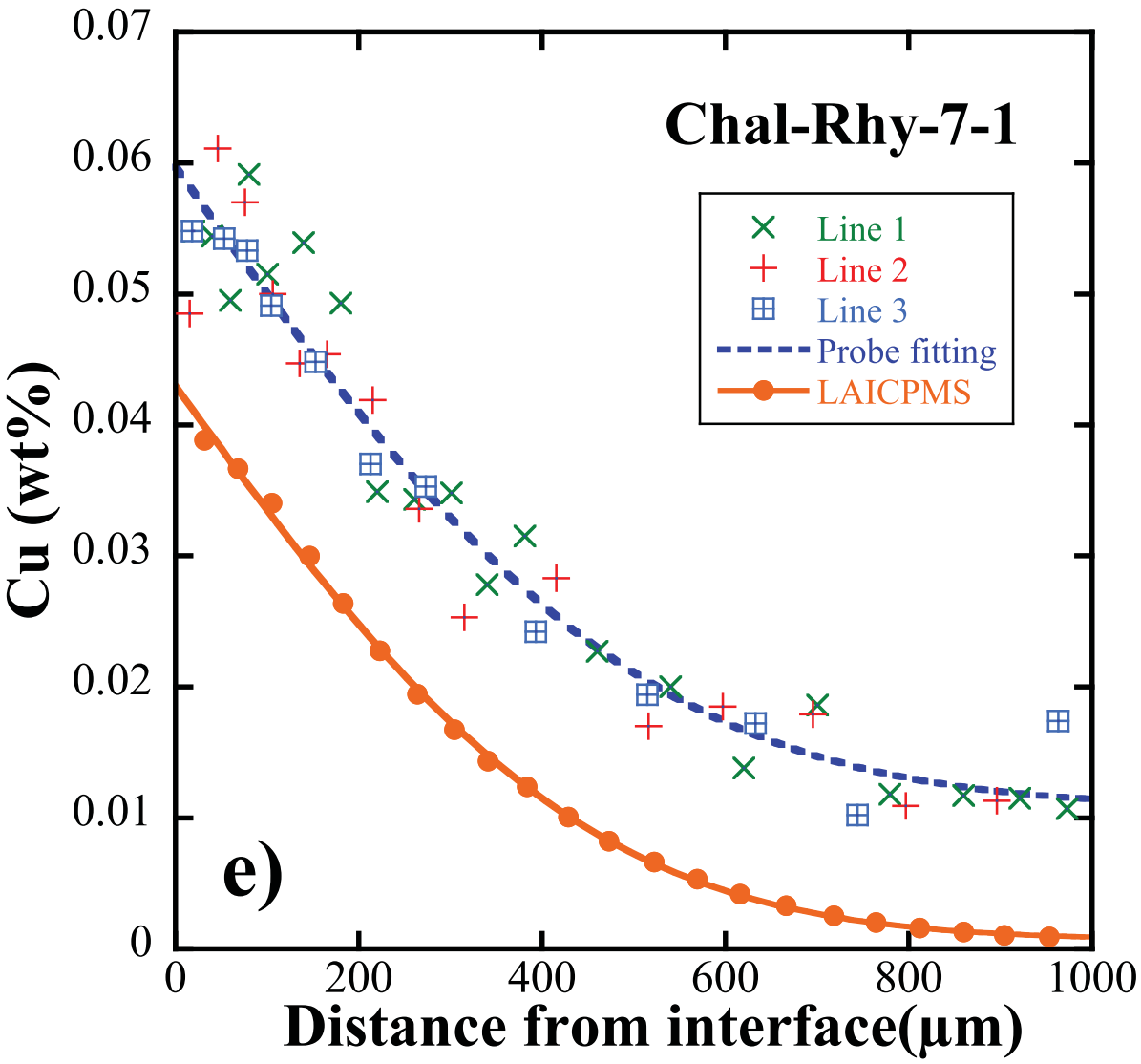

This is a preprint, the final version is subject to change, of the American Mineralogist (MSA)
Cite as Authors (Year) Title. American Mineralogist, in press.
(DOI will not work until issue is live.) DOI: http://dx.doi.org/10.2138/am-2017-5885

Fig.6f

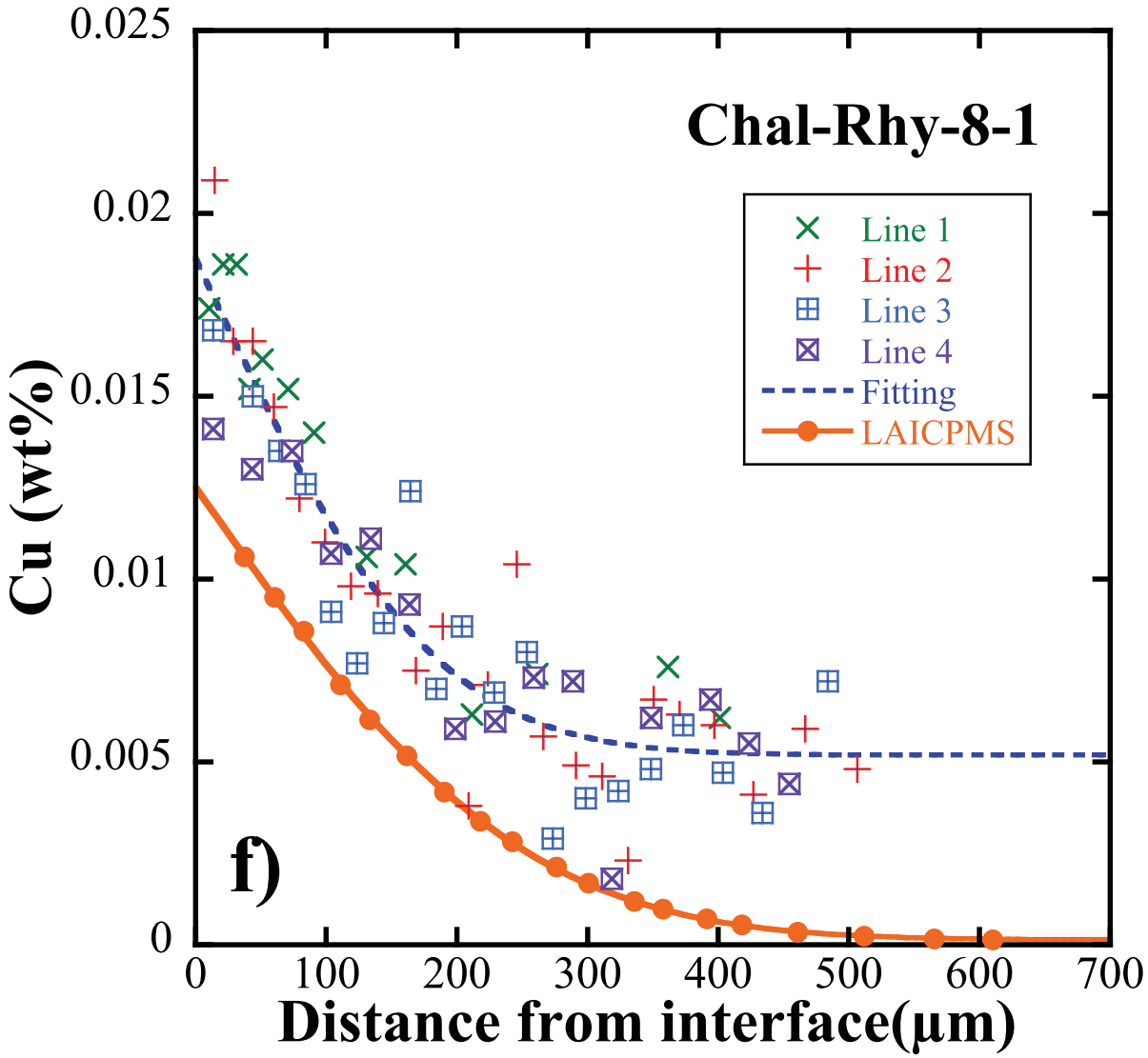

This is a preprint, the final version is subject to change, of the American Mineralogist (MSA)
Cite as Authors (Year) Title. American Mineralogist, in press.
(DOI will not work until issue is live.) DOI: http://dx.doi.org/10.2138/am-2017-5885

Fig.6g

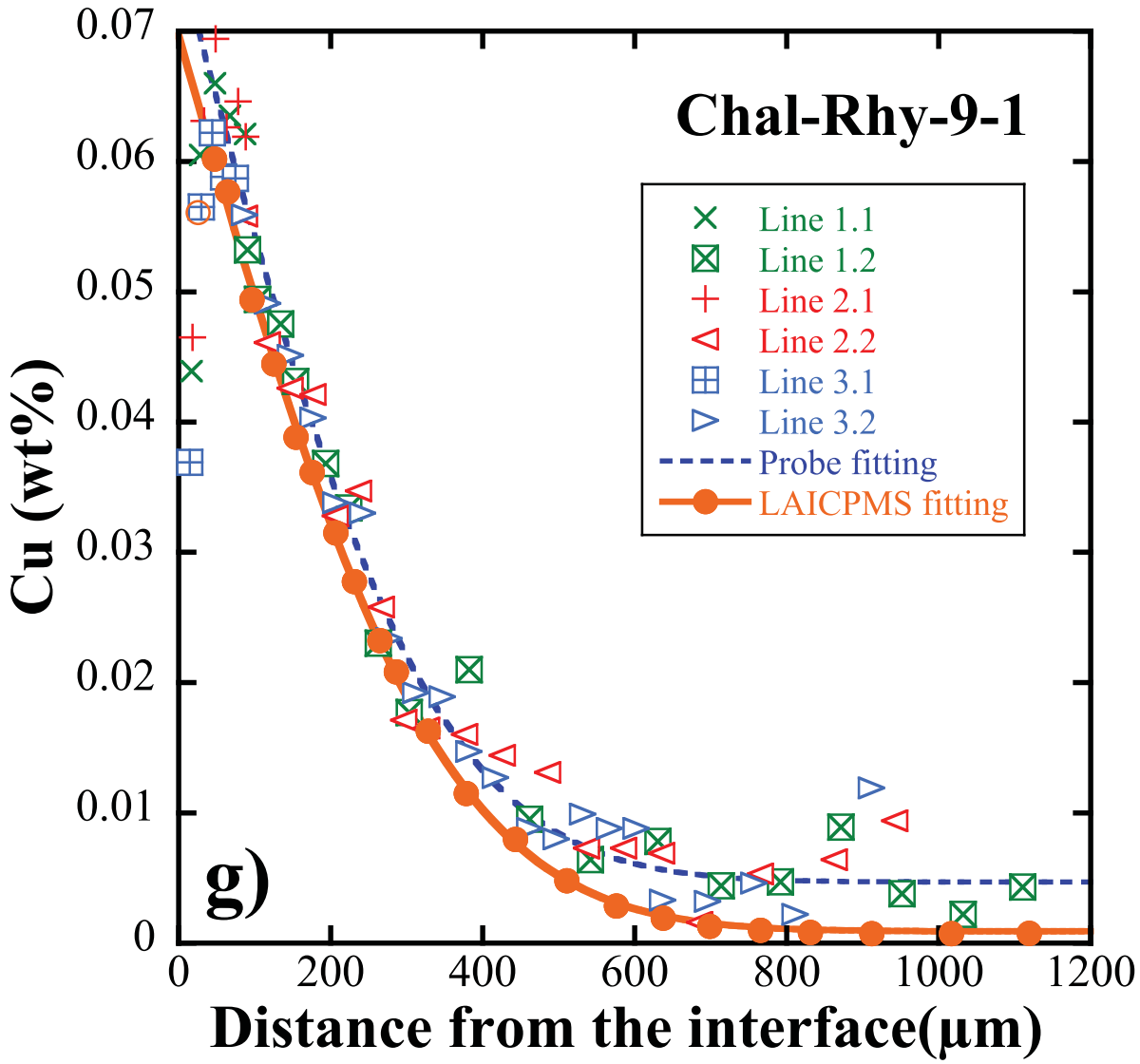

This is a preprint, the final version is subject to change, of the American Mineralogist (MSA)
Cite as Authors (Year) Title. American Mineralogist, in press.
(DOI will not work until issue is live.) DOI: http://dx.doi.org/10.2138/am-2017-5885

Fig.6h

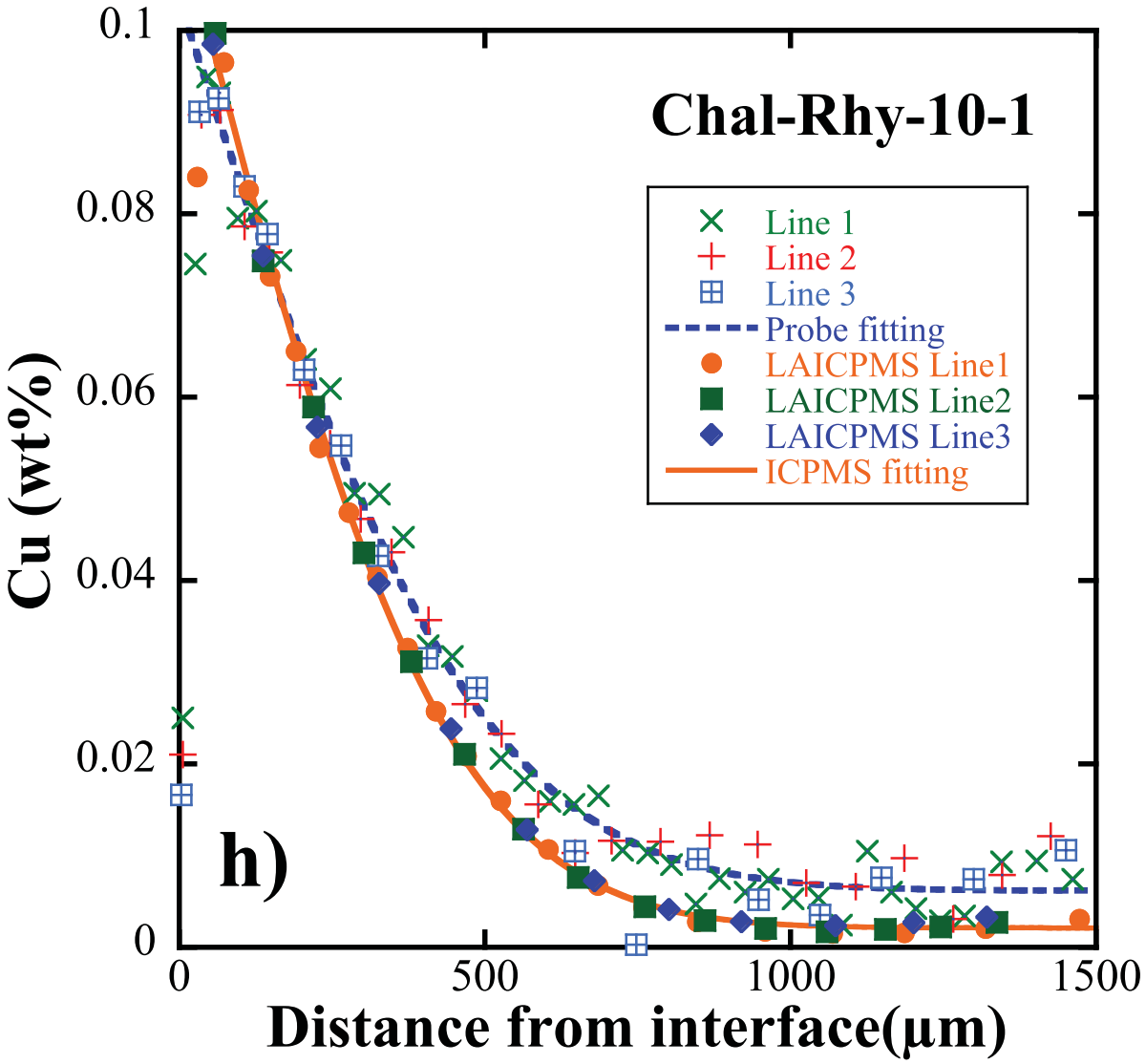

This is a preprint, the final version is subject to change, of the American Mineralogist (MSA)
Cite as Authors (Year) Title. American Mineralogist, in press.
(DOI will not work until issue is live.) DOI: http://dx.doi.org/10.2138/am-2017-5885

Fig.6i

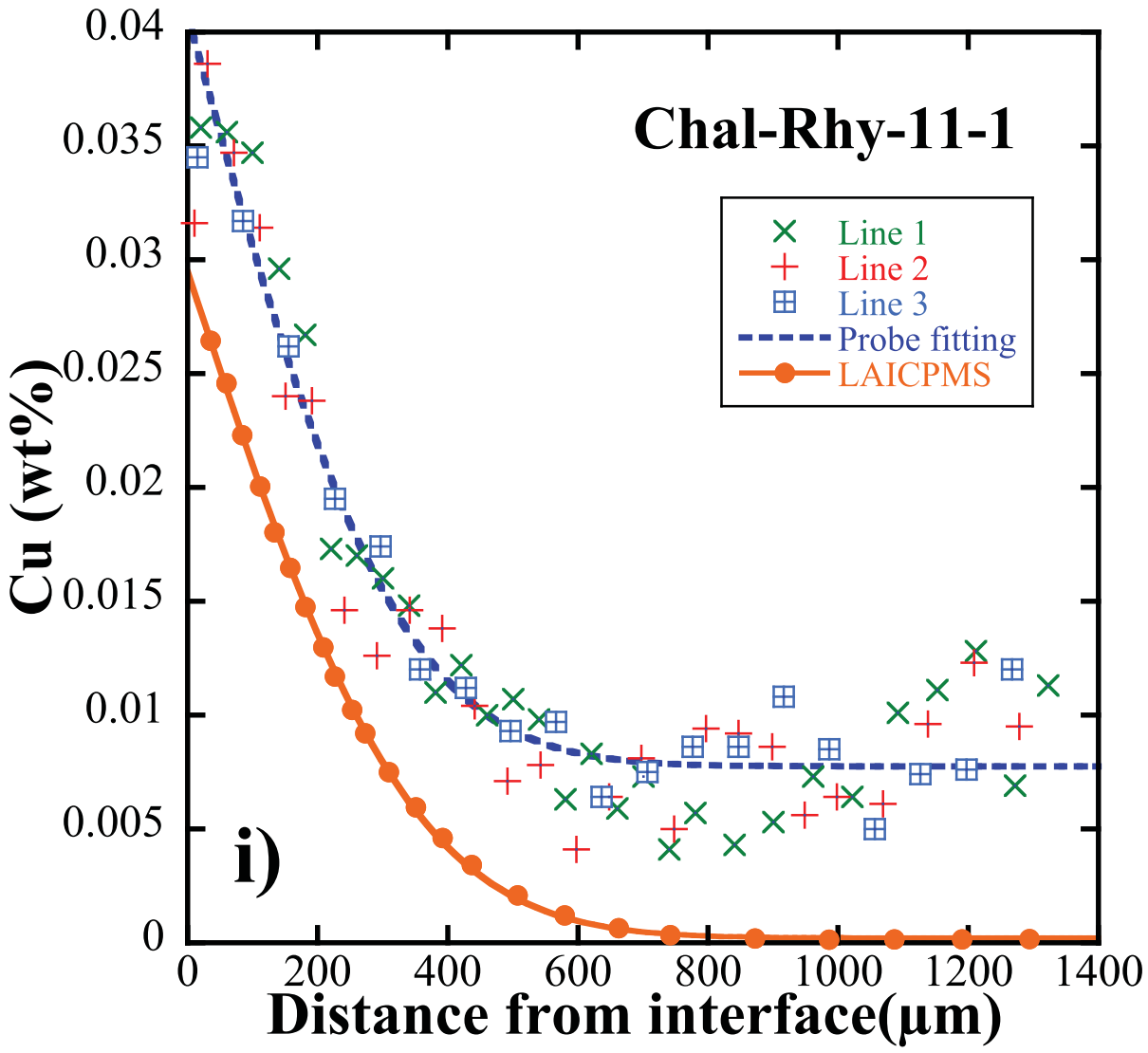

This is a preprint, the final version is subject to change, of the American Mineralogist (MSA)
Cite as Authors (Year) Title. American Mineralogist, in press.
(DOI will not work until issue is live.) DOI: http://dx.doi.org/10.2138/am-2017-5885

Fig.6j

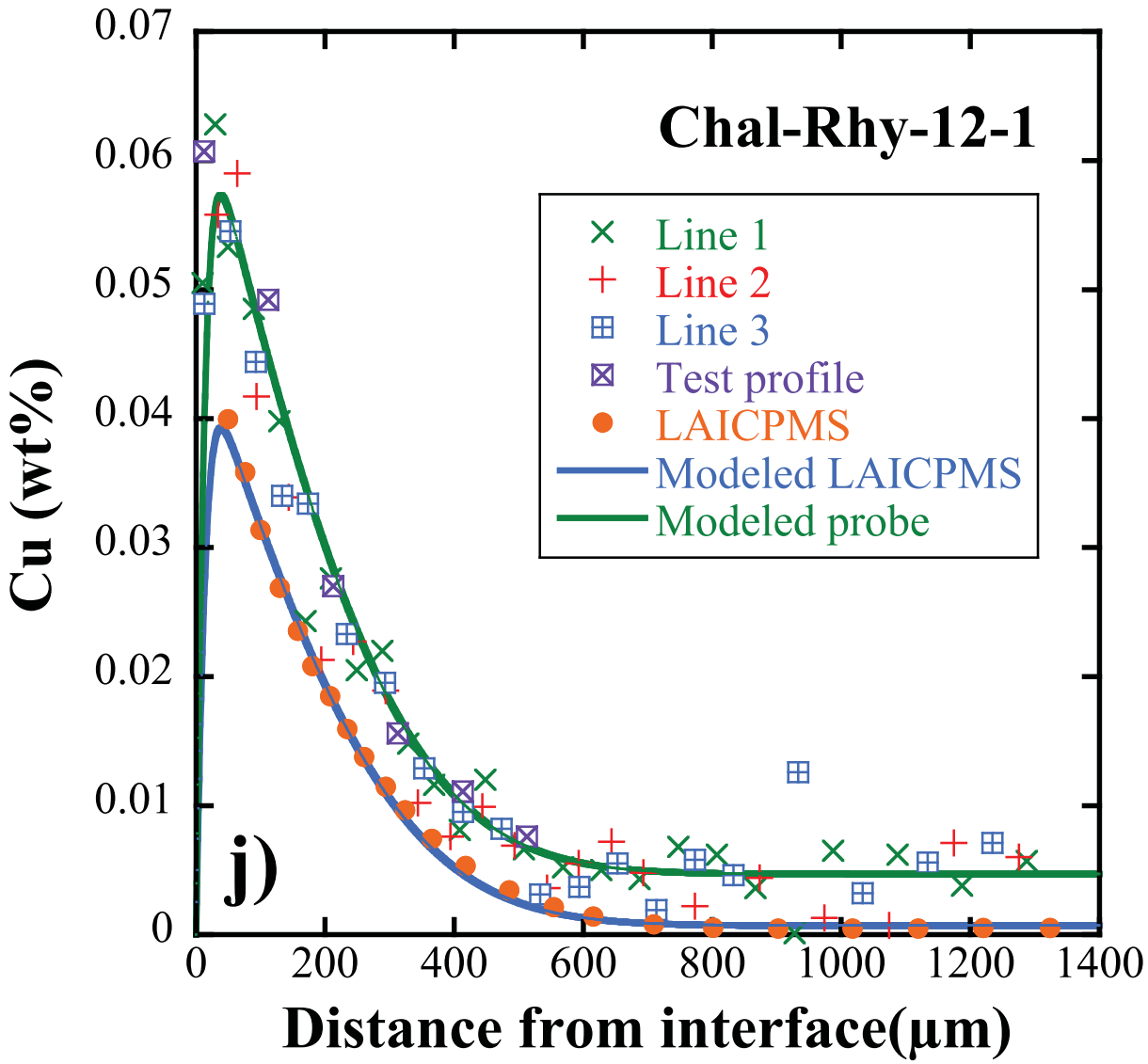

This is a preprint, the final version is subject to change, of the American Mineralogist (MSA)
Cite as Authors (Year) Title. American Mineralogist, in press.
(DOI will not work until issue is live.) DOI: http://dx.doi.org/10.2138/am-2017-5885

Fig.6k

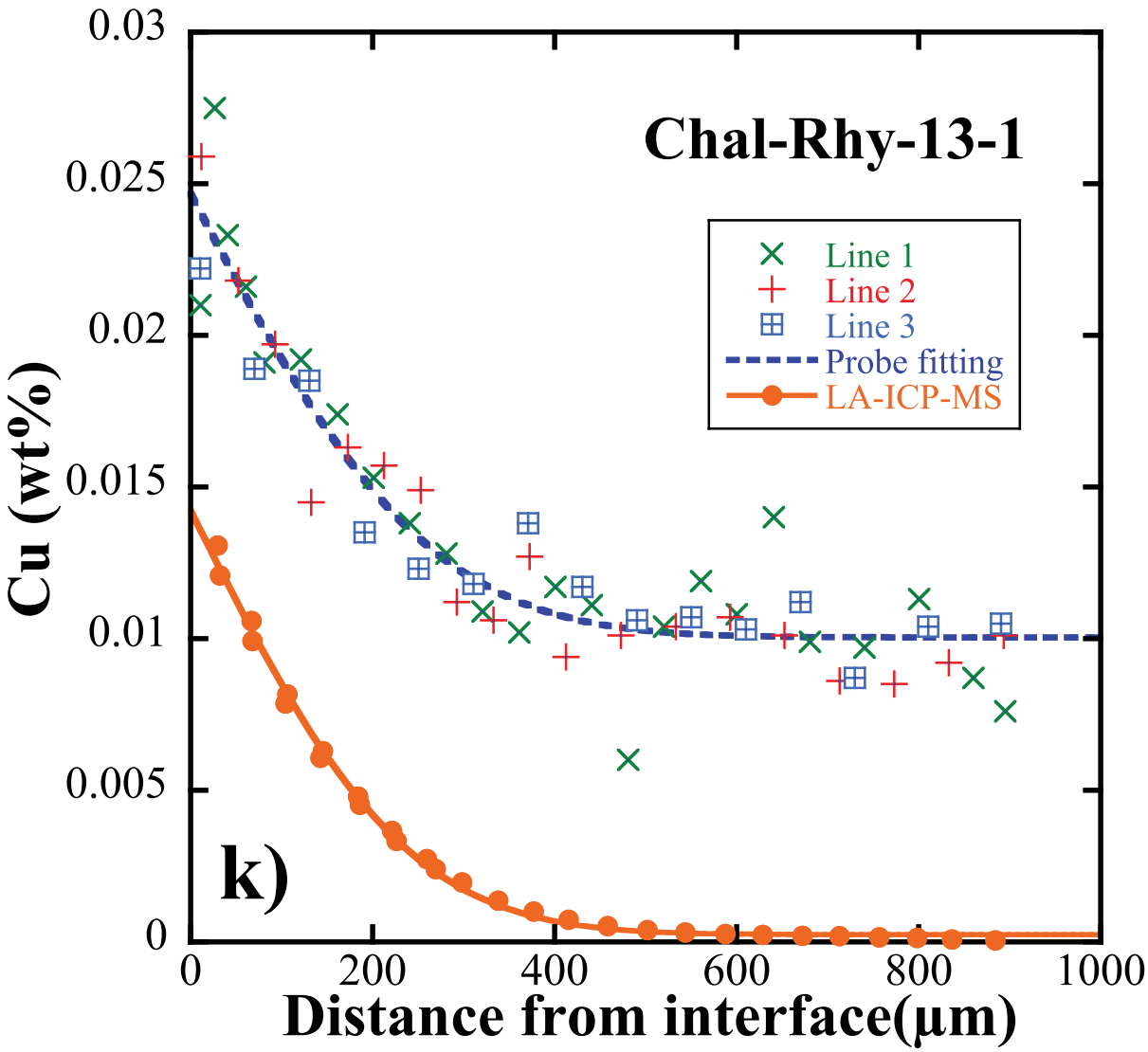

This is a preprint, the final version is subject to change, of the American Mineralogist (MSA)
Cite as Authors (Year) Title. American Mineralogist, in press.
(DOI will not work until issue is live.) DOI: http://dx.doi.org/10.2138/am-2017-5885

Fig.6l

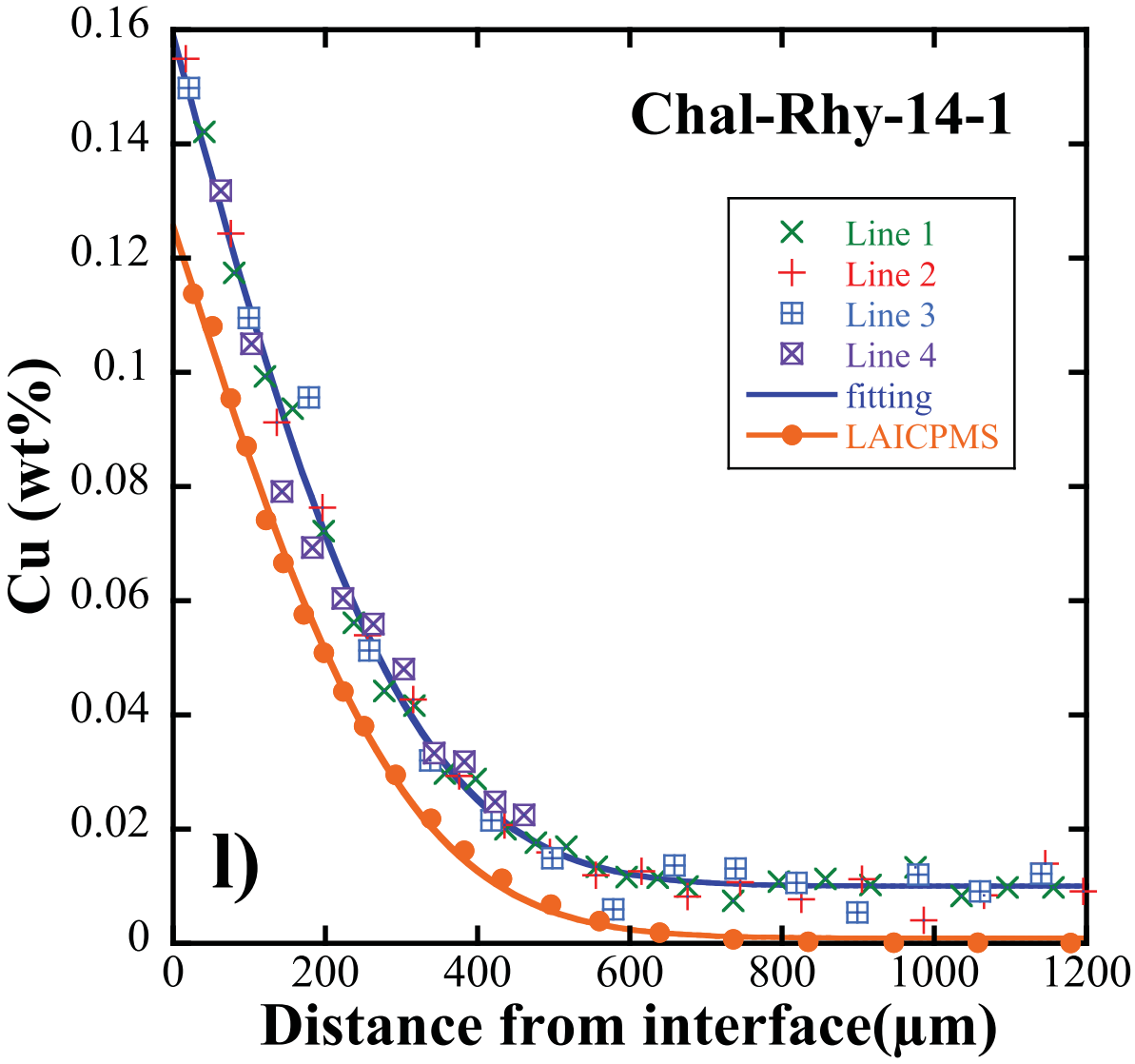

This is a preprint, the final version is subject to change, of the American Mineralogist (MSA)
Cite as Authors (Year) Title. American Mineralogist, in press.
(DOI will not work until issue is live.) DOI: http://dx.doi.org/10.2138/am-2017-5885

Fig.7a

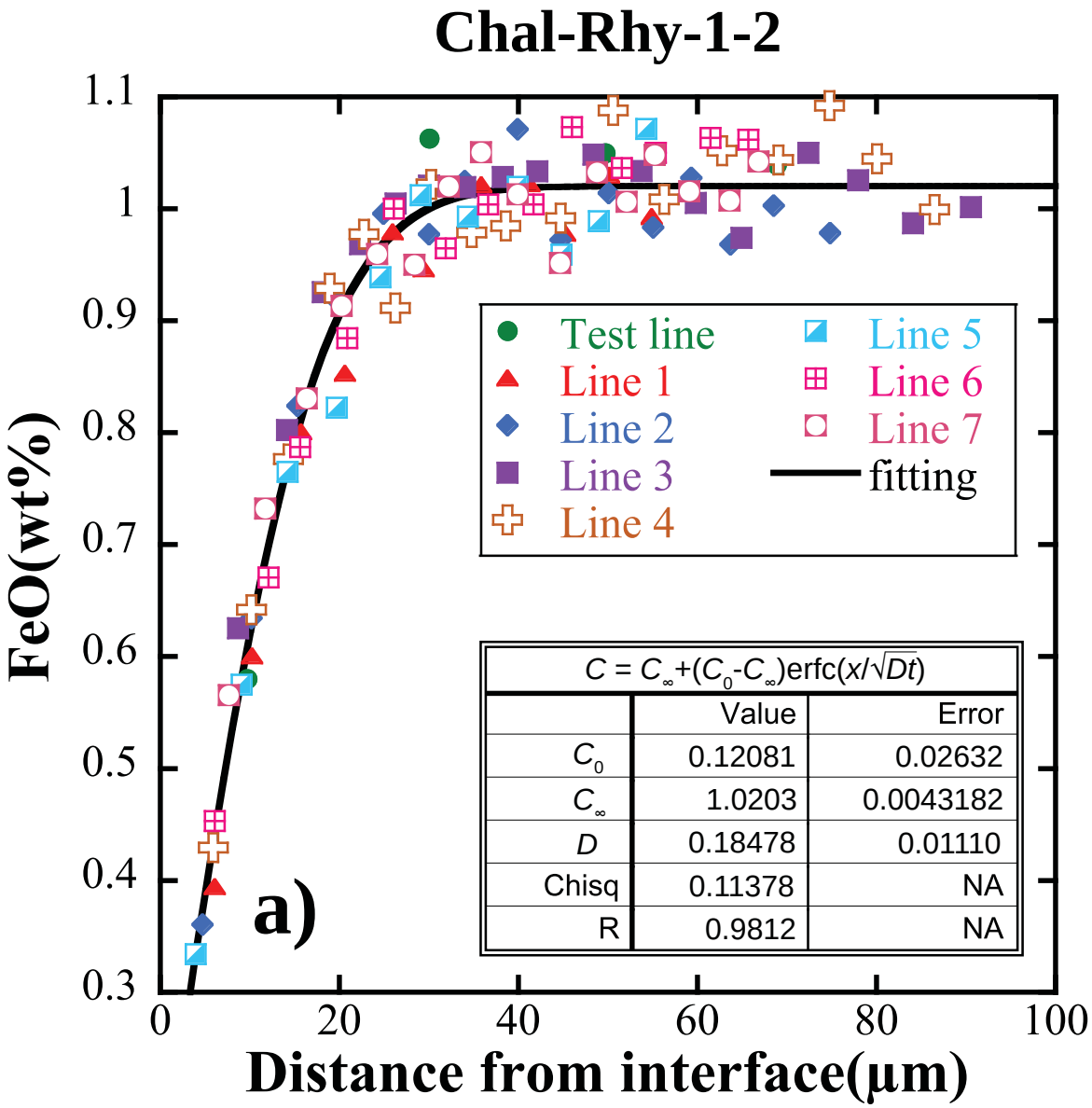

This is a preprint, the final version is subject to change, of the American Mineralogist (MSA)
Cite as Authors (Year) Title. American Mineralogist, in press.
(DOI will not work until issue is live.) DOI: http://dx.doi.org/10.2138/am-2017-5885

Fig.7b

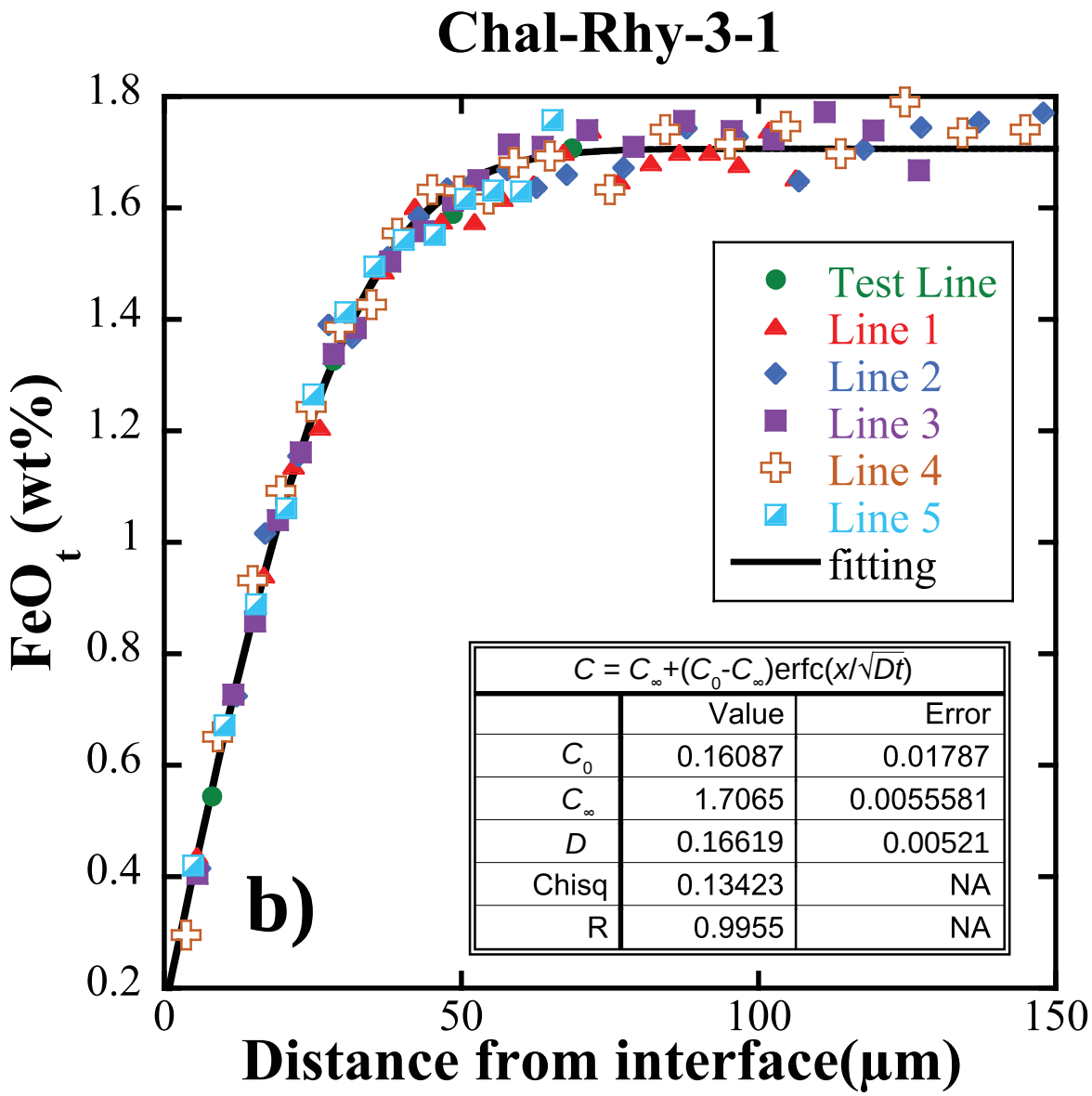

This is a preprint, the final version is subject to change, of the American Mineralogist (MSA)
Cite as Authors (Year) Title. American Mineralogist, in press.
(DOI will not work until issue is live.) DOI: http://dx.doi.org/10.2138/am-2017-5885

Fig.7c

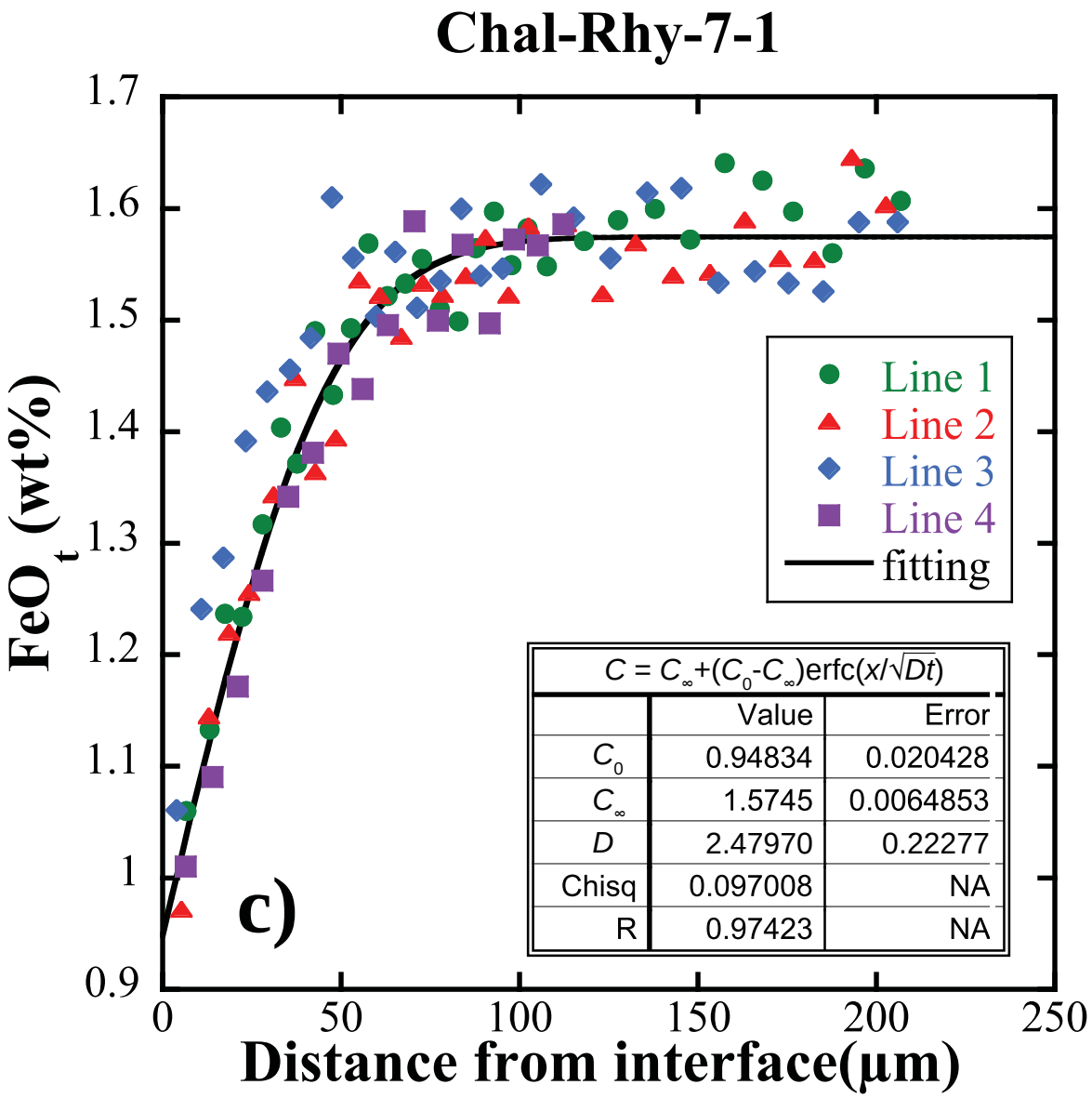

This is a preprint, the final version is subject to change, of the American Mineralogist (MSA)
Cite as Authors (Year) Title. American Mineralogist, in press.
(DOI will not work until issue is live.) DOI: http://dx.doi.org/10.2138/am-2017-5885

Fig.7d

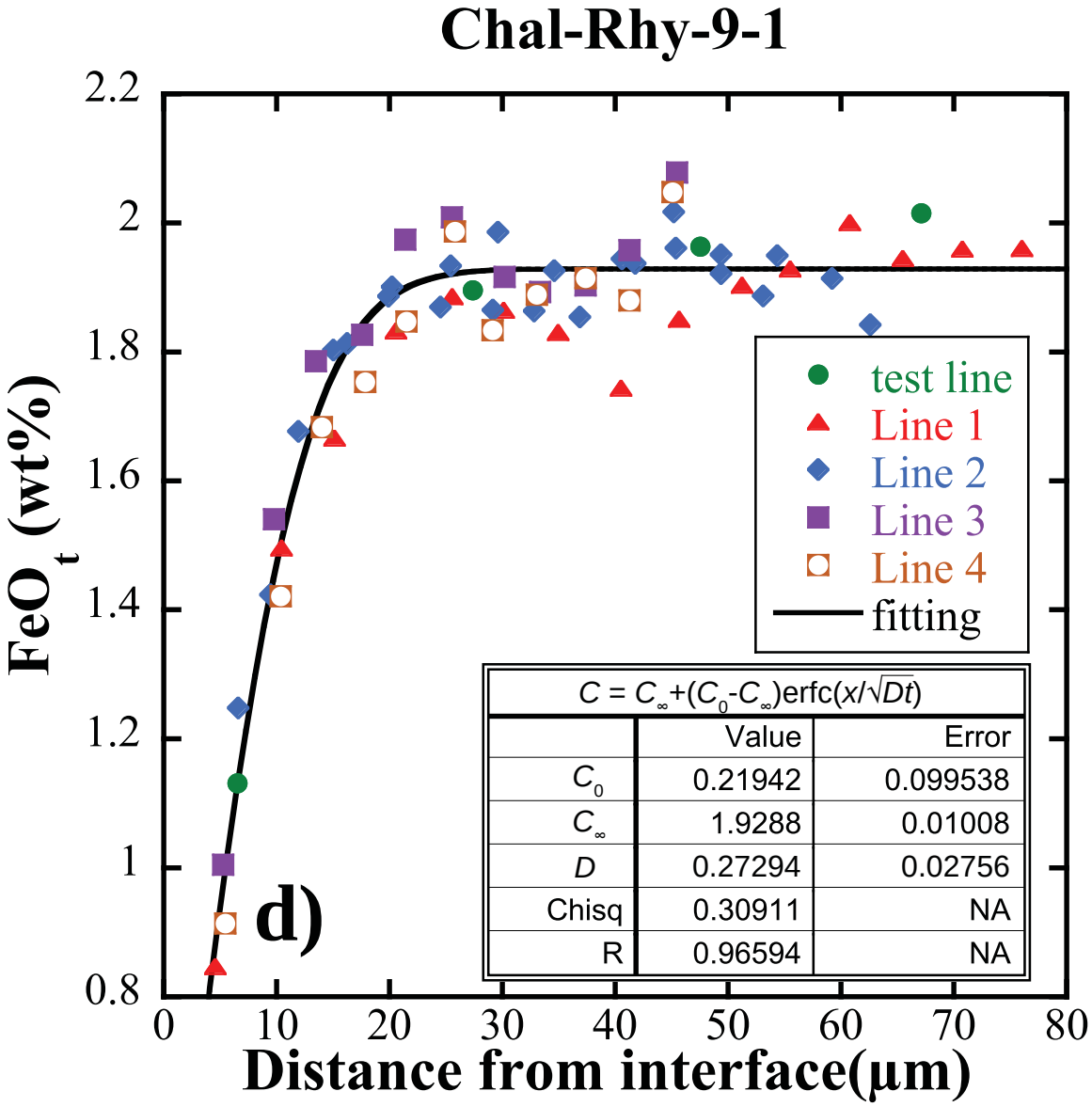

This is a preprint, the final version is subject to change, of the American Mineralogist (MSA)
Cite as Authors (Year) Title. American Mineralogist, in press.
(DOI will not work until issue is live.) DOI: http://dx.doi.org/10.2138/am-2017-5885

Fig.7e

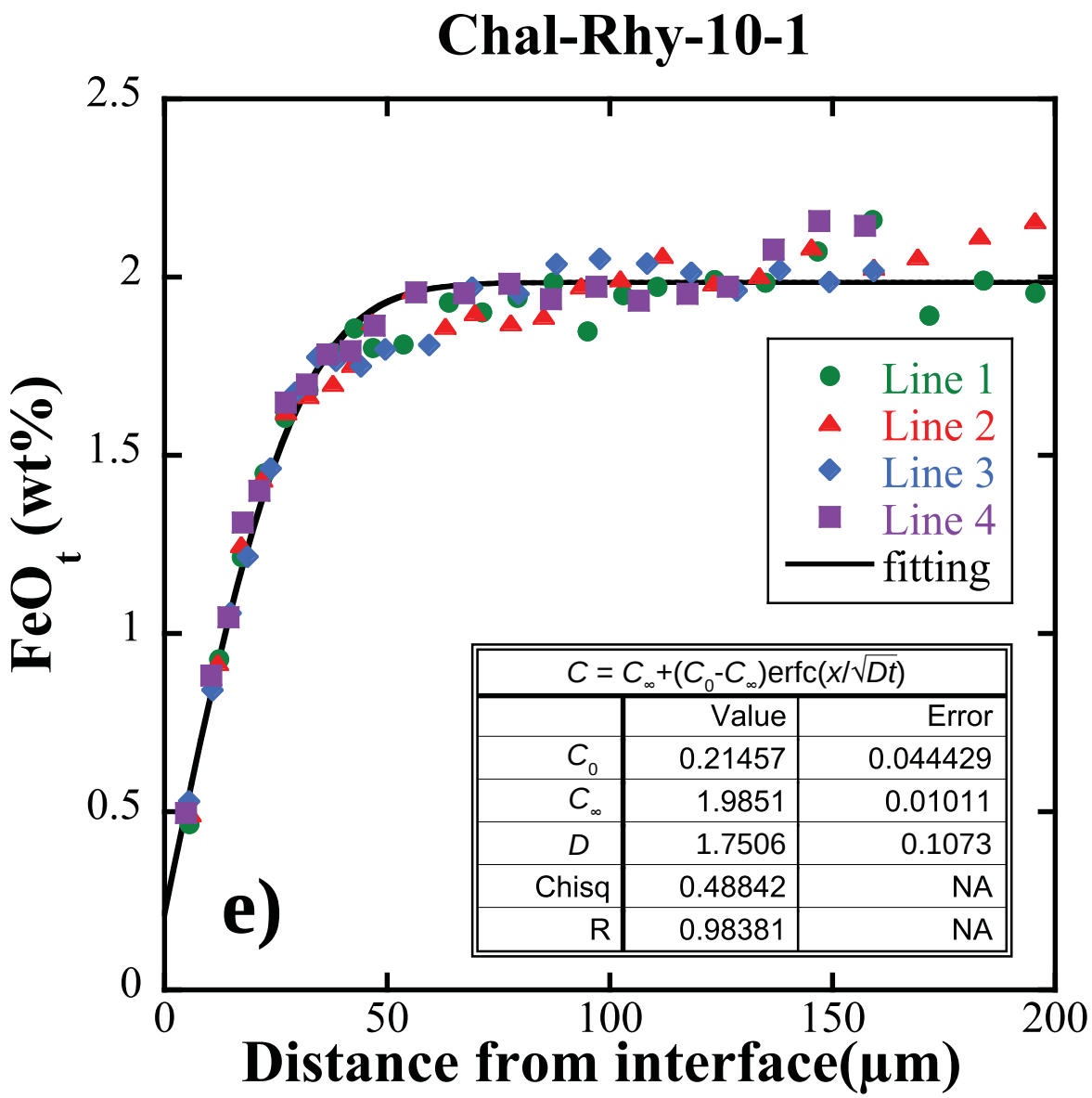

This is a preprint, the final version is subject to change, of the American Mineralogist (MSA)
Cite as Authors (Year) Title. American Mineralogist, in press.
(DOI will not work until issue is live.) DOI: http://dx.doi.org/10.2138/am-2017-5885

Fig.7f

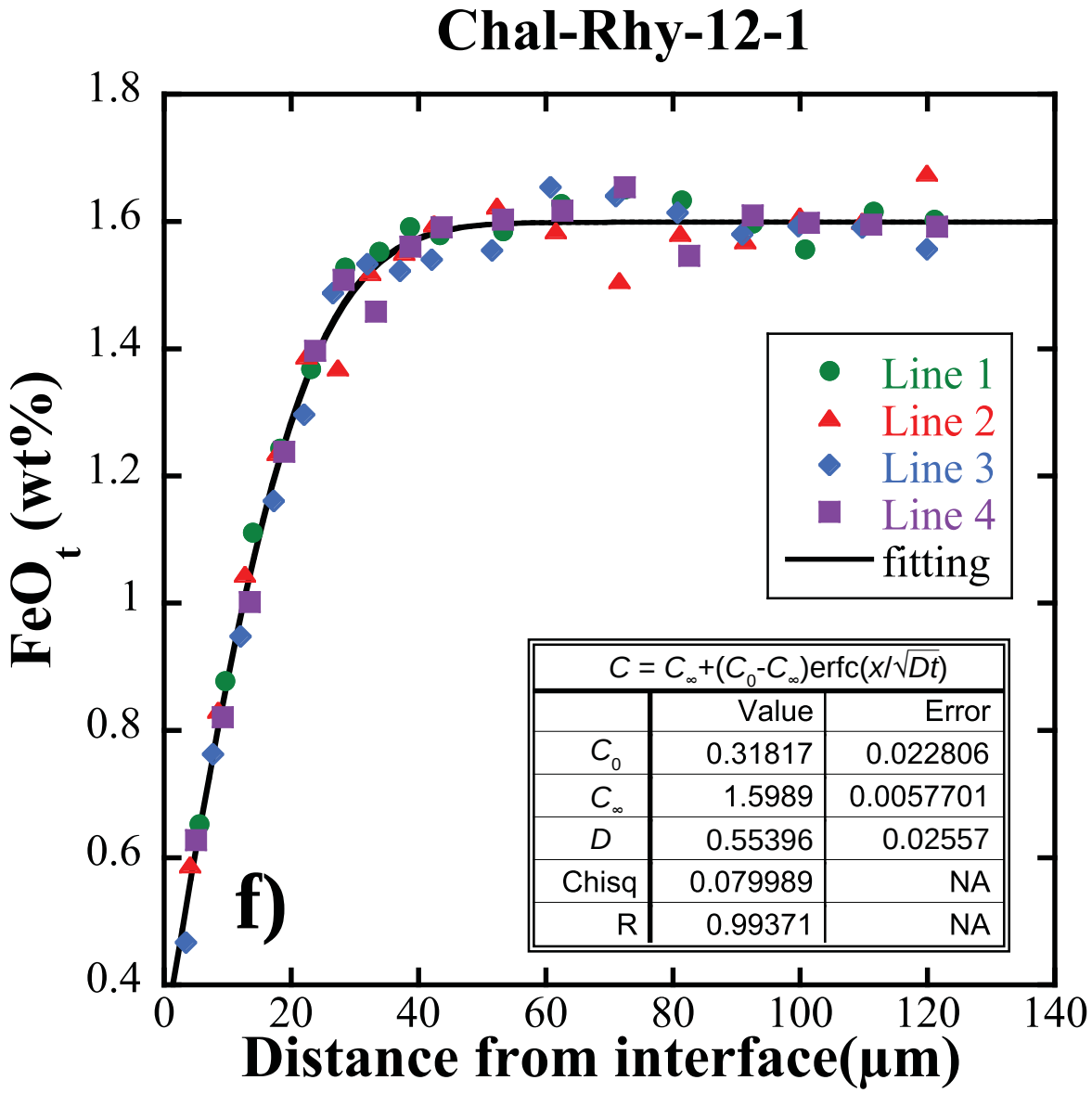

This is a preprint, the final version is subject to change, of the American Mineralogist (MSA)
Cite as Authors (Year) Title. American Mineralogist, in press.
(DOI will not work until issue is live.) DOI: http://dx.doi.org/10.2138/am-2017-5885

Fig.7g

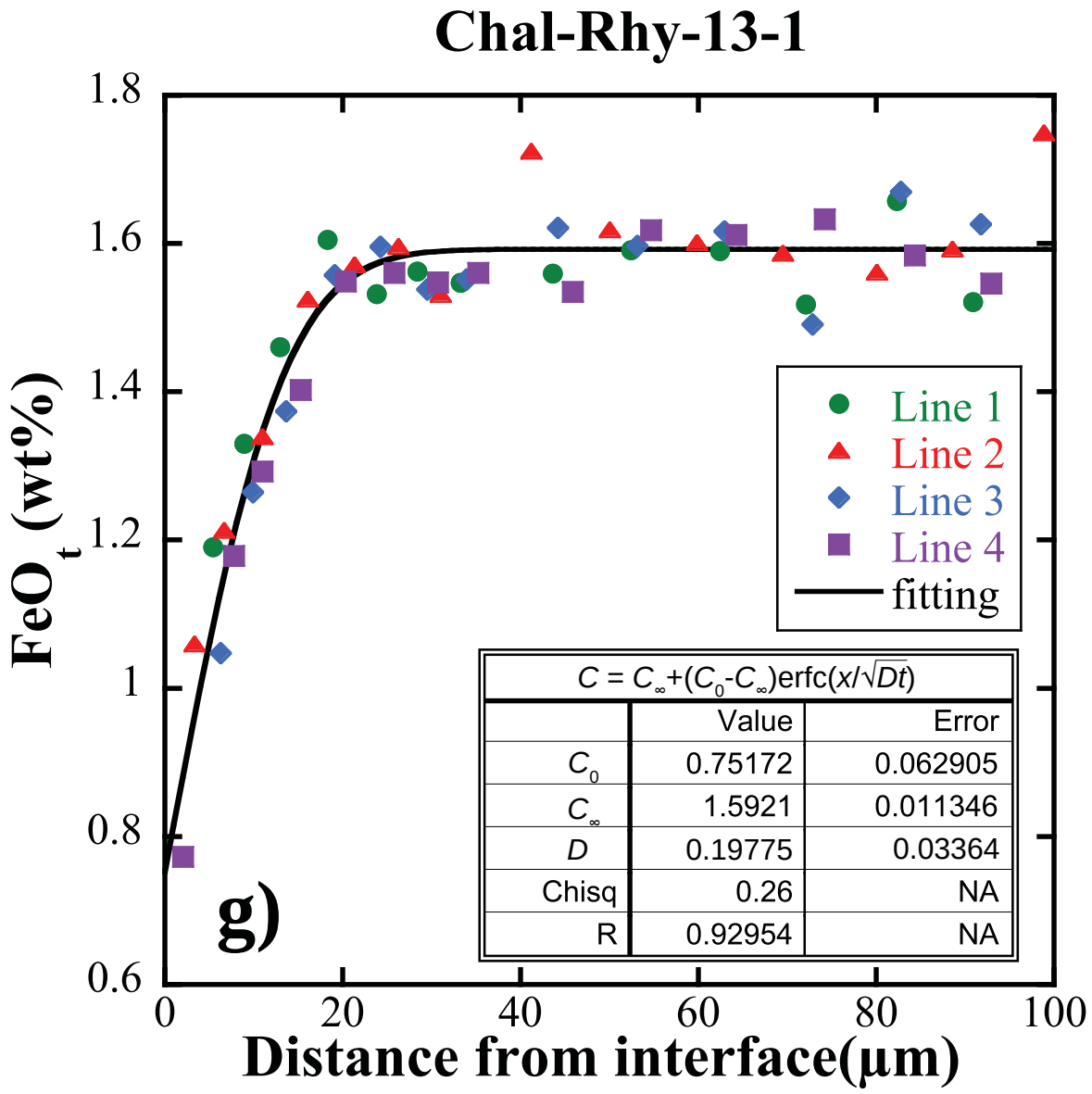

This is a preprint, the final version is subject to change, of the American Mineralogist (MSA)
Cite as Authors (Year) Title. American Mineralogist, in press.
(DOI will not work until issue is live.) DOI: http://dx.doi.org/10.2138/am-2017-5885

Fig.8a

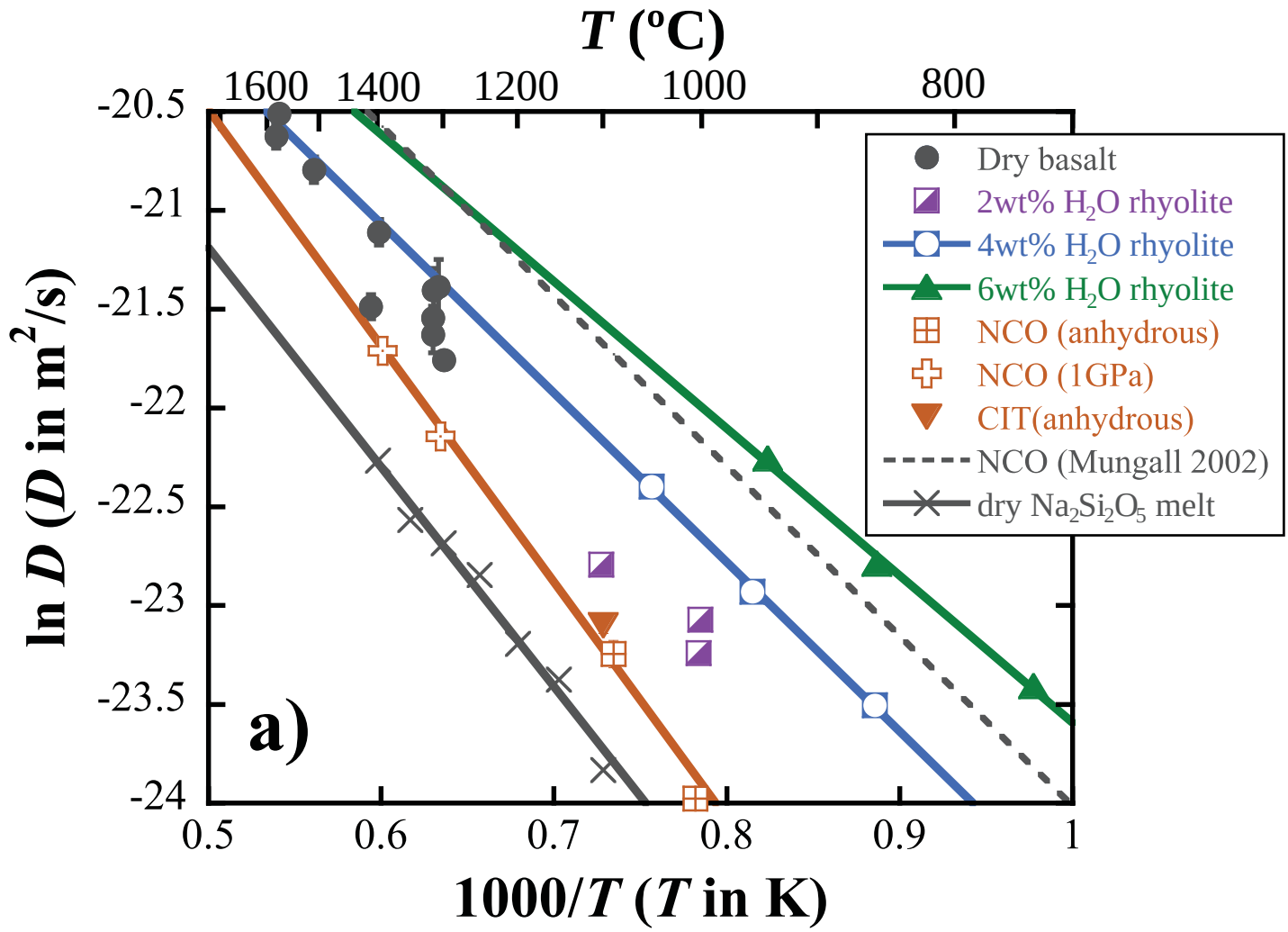

This is a preprint, the final version is subject to change, of the American Mineralogist (MSA)
Cite as Authors (Year) Title. American Mineralogist, in press.
(DOI will not work until issue is live.) DOI: http://dx.doi.org/10.2138/am-2017-5885

Fig.8b

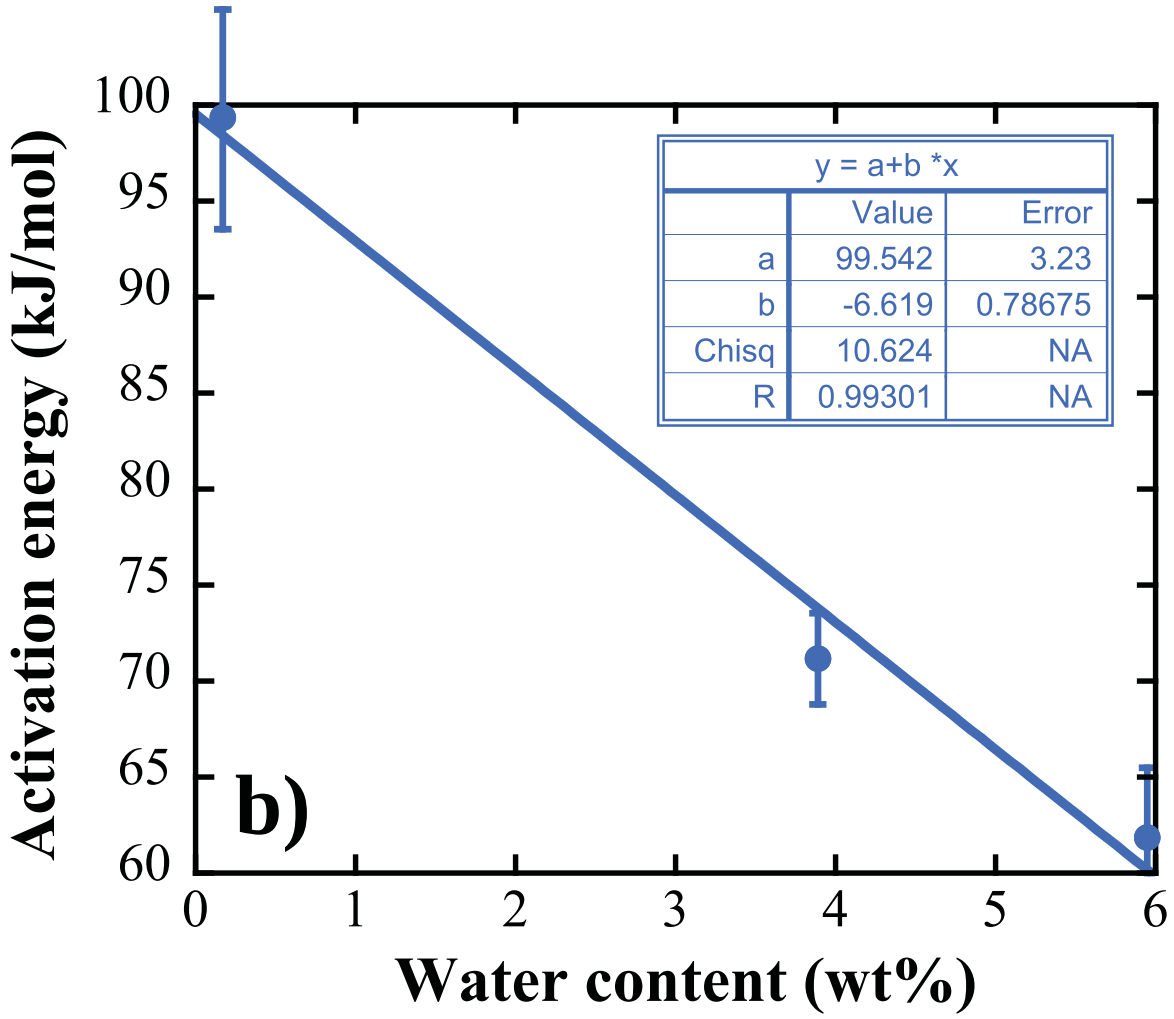

This is a preprint, the final version is subject to change, of the American Mineralogist (MSA)
Cite as Authors (Year) Title. American Mineralogist, in press.
(DOI will not work until issue is live.) DOI: http://dx.doi.org/10.2138/am-2017-5885

Fig.9

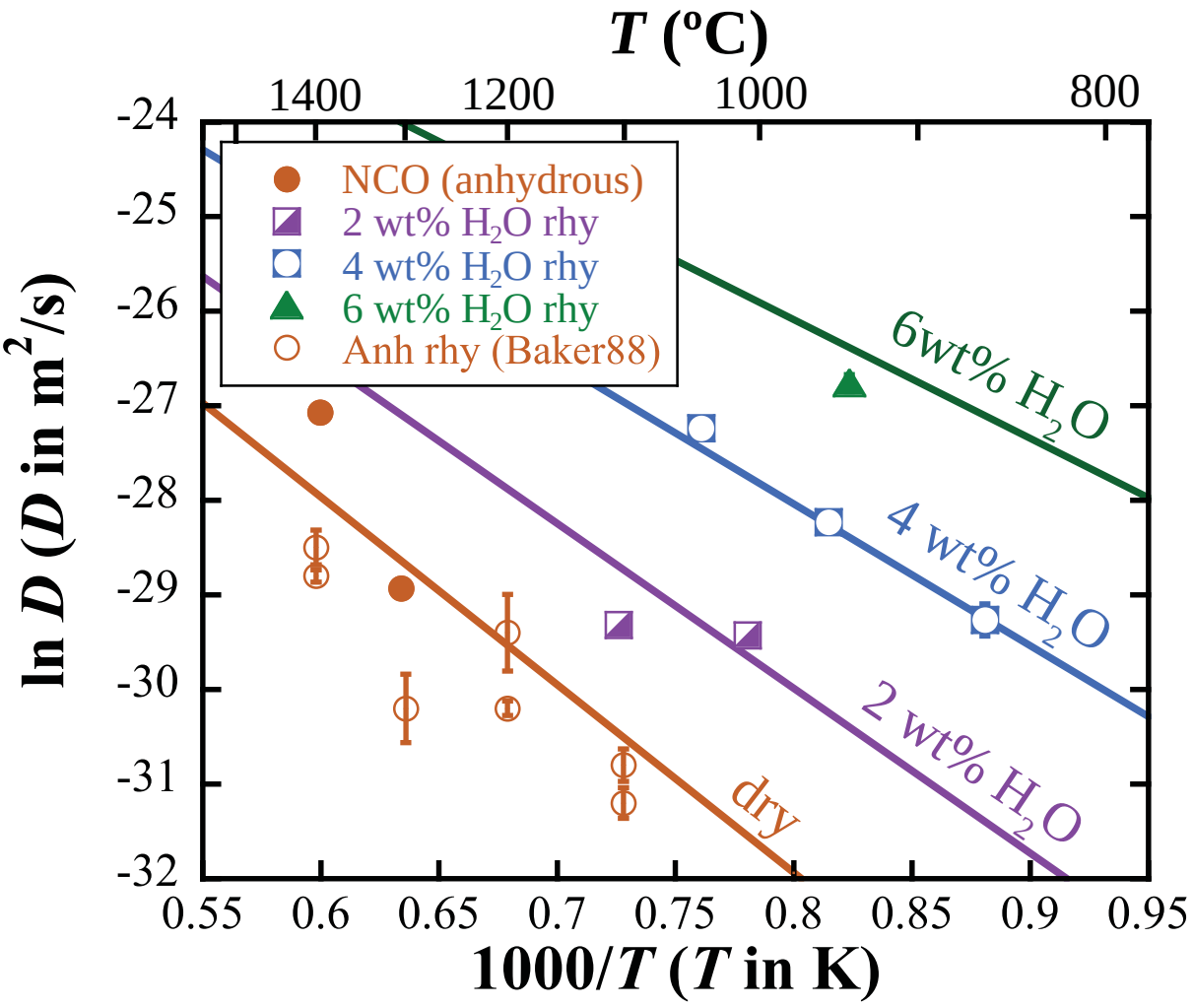

This is a preprint, the final version is subject to change, of the American Mineralogist (MSA)
Cite as Authors (Year) Title. American Mineralogist, in press.
(DOI will not work until issue is live.) DOI: http://dx.doi.org/10.2138/am-2017-5885

Fig.10